

NASA Contractor Report 4457
DOT/FAA/RD-92/21

Spectrum Modal Analysis for the Detection of Low-Altitude Windshear With Airborne Doppler Radar

Matthew W. Kunkel
Radar Systems Laboratory
Electrical and Computer Engineering Department
Clemson University
Clemson, South Carolina

Prepared for
Langley Research Center
under Grant NAG1-928



National Aeronautics and
Space Administration
Office of Management
Scientific and Technical
Information Program

1992

TABLE OF CONTENTS

	Page
LIST OF FIGURES	v
ACKNOWLEDGMENTS	vii
CHAPTER	
1. INTRODUCTION	1
The Microburst	1
Windspeed Gradient	1
Hazard Factor	3
Hazard Factor Algorithm	5
Doppler Weather Radar	7
Problem Statement	11
2. WINDSPEED ESTIMATION	12
Time Domain Pulse-Pair Mean and Width Estimator	12
Frequency Domain Pulse-Pair Mean and Width Estimator	13
Spectral Domain Mean-Variance Mean and Width Estimator	14
The Effect of Clutter on Windspeed Estimates	15
Clutter Rejection Filters	16
3. SPECTRAL ESTIMATION USING MODAL ANALYSIS	17
The Prony Approach	18
Extended Prony Analysis	20
Second Order Extended Prony Analysis	20
4. WINDSPEED ESTIMATION FROM A TWO POLE MODEL	27
Characterizing the Poles	27
Pole Spreading Effect from AR Modeling	31
Two Class Pattern Recognition Technique	33
Second Coefficient Windspeed Estimator	43

PRECEDING PAGE BLANK NOT FILMED



Table of Contents (Continued)

	Page
5. RESULTS	47
Comparison of Windspeed Estimates	48
Comparison of Hazard Factors	56
Fixed Range Time Scan	57
6. CONCLUSIONS	66
APPENDICES	68
A. Autoregressive Modeling	69
B. Windspeed Estimates by Frame	71
C. NASA Model Parameters	86
REFERENCES	88

LIST OF FIGURES

Figure	Page
1.1 Symmetric Microburst	2
1.2 “S”-curve Pattern of a Typical Microburst	4
3.1 Second Order AR Spectral Estimate and Pole Locations	23
3.2 Bubble Plot of Velocity Estimates for a Microburst Event	25
4.1 20th Order AR Spectra for a Simulated Microburst and Clutter Return	29
4.2 20th Order AR Spectra for a Simulated Clutter Only Return	29
4.3 Bubble Plot for Simulated Microburst and Clutter Return	30
4.4 Bubble Plot for Simulated Clutter Only Return	30
4.5 Bubble Plot for Third Order Simulated Clutter Only Return	32
4.6 Complex Values of Pole 1 for Simulated Microburst and Clutter Return	35
4.7 Complex Values of Pole 1 for Simulated Clutter Only Return	35
4.8 Complex Values of Pole 2 for Simulated Microburst and Clutter Return	36
4.9 Complex Values of Pole 2 for Simulated Clutter Only Return	36
4.10 Polar Values of Pole 1 for Simulated Microburst and Clutter Return	38
4.11 Polar Values of Pole 1 for Simulated Clutter Only Return	38
4.12 Polar Values of Pole 2 for Simulated Microburst and Clutter Return	39
4.13 Polar Values of Pole 2 for Simulated Clutter Only Return	39
4.14 Polar Values of Pole 1 for 10 Simulated Microburst and Clutter Returns	41
4.15 Polar Values of Pole 1 for 10 Simulated Clutter Only Returns	41
4.16 Two Class Pattern Recognition Windspeed Estimator	42

List of Figures (Continued)

	Page
4.17 Bubble Plot with Windspeed Estimates for Microburst and Clutter	44
4.18 Bubble Plot with Windspeed Estimates for Clutter Only	44
4.19 Second Coefficient Windspeed Estimator	46
5.1 Pulse-Pair Velocity Estimates for Event 143	49
5.2 Pulse-Pair Velocity Estimates for Event 143, smoothed	49
5.3 Pole 1 Values for Event 143	51
5.4 Two Pole Classification Estimates for Event 143	52
5.5 Two Pole Classification Estimates for Event 143, smoothed	52
5.6 Values of Second AR Coefficient for Event 143	54
5.7 Second Coefficient Velocity Estimates for Event 143	55
5.8 Second Coefficient Velocity Estimates for Event 143, smoothed	55
5.9 Pulse-Pair Hazard Factor for Event 143	58
5.10 Contour of Pulse-Pair Hazard Factor for Event 143	58
5.11 Two Pole Classifier Hazard Factor for Event 143	59
5.12 Contour of Two Pole Classifier Hazard Factor for Event 143	59
5.13 Second Coefficient Classifier Hazard Factor for Event 143	60
5.14 Contour of Second Coefficient Classifier Hazard Factor for Event 143	60
5.15 Snapshot	62
5.16 Fixed Range Time Scan	62
5.17 Illustration of Snapshot Processing	63
5.18 Illustration of Fixed Range Processing	64

ACKNOWLEDGMENTS

The author wishes to extend his sincere appreciation to all those helping him throughout his graduate studies. Foremost is his major advisor, Dr. E. G. Baxa, Jr., whose advice and support made this thesis possible. He would also like to thank the other members of his committee, Dr. R. J. Schalkoff and Dr. C. Jeffries, for their time and contributions. In addition, recognition is given to the National Aeronautics and Space Administration for their financial support under grant No. NAG-1-928 and to the Antenna and Microwave Research Branch at Langley research Center for technical support.

The author would also like to thank the students of the Radar Systems Laboratory at Clemson University for their advice and technical contributions. Finally, he wishes to thank his family for their immeasurable support. Special thanks are extended to his parents whose encouragement made this possible and to Rhonda Mathis whose love and support has been unfaltering throughout his graduate studies.

CHAPTER 1

INTRODUCTION

1.1 The Microburst

The term downburst was used by T. Theodore Fujita to describe a form of low-altitude windshear in which a downdraft of air impacts the ground and diverges into a horizontal outflow. Outflows with a radius greater than 4 km are called macrobursts while events with smaller outflows are called microbursts [1]. Low-altitude microbursts have been recognized as a hazard to aviation for aircrafts attempting to fly through this event. An aircraft encountering a microburst will first experience a performance increasing headwind as it enters the forward outflow, but encounters a strong downdraft as it approaches the center of the microburst. The performance decrease caused by the downdraft is further increased by the tailwind created as the aircraft flies out of the microburst. In some cases the performance decrease caused by such an event would render an escape impossible. A microburst event is represented in Figure 1.1.

1.2 Windspeed Gradient

Typical procedures for airborne windshear detection rely on the estimation of the windfield characteristics present within a region of space positioned in front of the aircraft. This space represents the region of possible flight paths for the aircraft. A potentially hazardous condition exists in the forward-looking direction when there is a large headwind-to-tailwind gradient in the windspeed. Such a gradient typically reflects the windspeed characteristics observed by an aircraft as it penetrates the outflow of a microburst event. A sampling of average windspeed measurements throughout the outflow region will typically follow a gradient in windspeed feature known as an “S”-curve pattern. An example “S”-curve is shown in Figure 1.2. Note the rapid

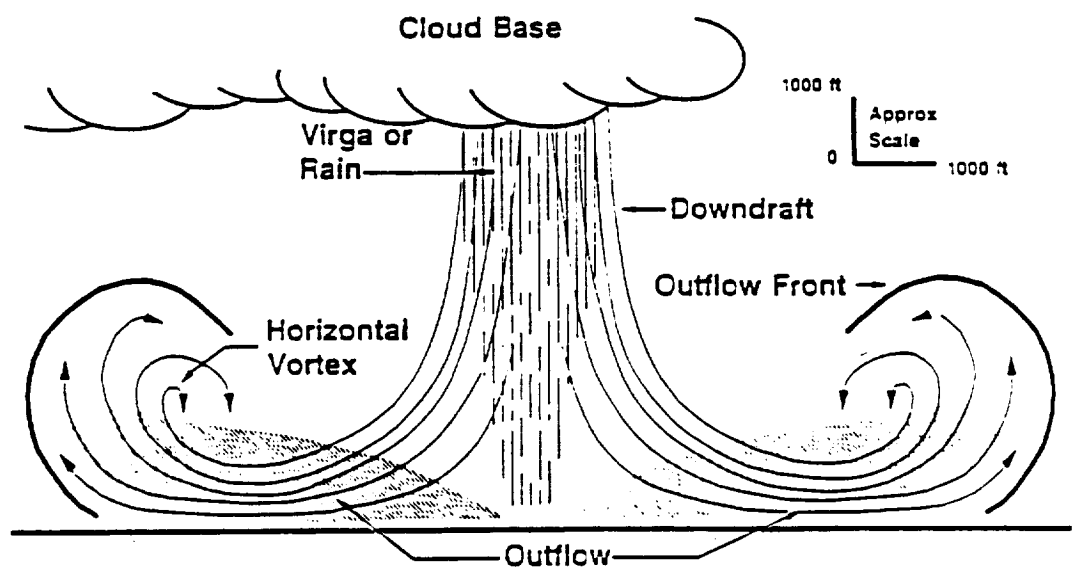


Figure 1.1 Symmetric Microburst

change from a negative windspeed (headwind), to a positive windspeed (tailwind). From these measured windspeed values, an attempt can be made to assign a value to the effect of the corresponding windfield conditions upon the performance level of the aircraft as it flies through the given region of space. One such measure of a hazardous situation has been defined in [2] in terms of a maximum windspeed divergence of over 10 meters per second (m/s) occurring in a region of less than 4 km.

It is important to note that the windfield estimates from forward-looking airborne sensors, such as pulse Doppler radar, LIDAR (Laser Interferometric Detection and Ranging) [3], and FLIR (forward looking infrared radiometer) [4] have only the ability to estimate radial (line-of-sight) windspeeds along the direction where the sensors are pointed. Current research continues on the ability of these systems to provide a reliable advanced warning of a windshear condition.

1.3 Hazard Factor

It is necessary to define a measure of the severity of a microburst in terms of its performance-decreasing effect on an aircraft flying through the event. The analysis involved in computing such an index relies upon the concept of airplane total energy which is the sum of the aircraft's kinetic and potential energy [3]. Temporally and spatially varying windfields will contribute to the rate of change of airplane total energy. Severe windfield events, such as a microburst, can significantly lower total energy to the point where the aircraft can no longer remain in the air.

Define the airplane total energy as

$$E = \frac{1}{2}m\nu^2 + hmg \quad (1.1)$$

where m is the mass of the aircraft, ν is airspeed, h is altitude, and g is acceleration due to gravity. The potential altitude is defined as energy per unit weight and is given by

$$h_p = \frac{E}{mg} = \frac{\nu^2}{2g} + h . \quad (1.2)$$

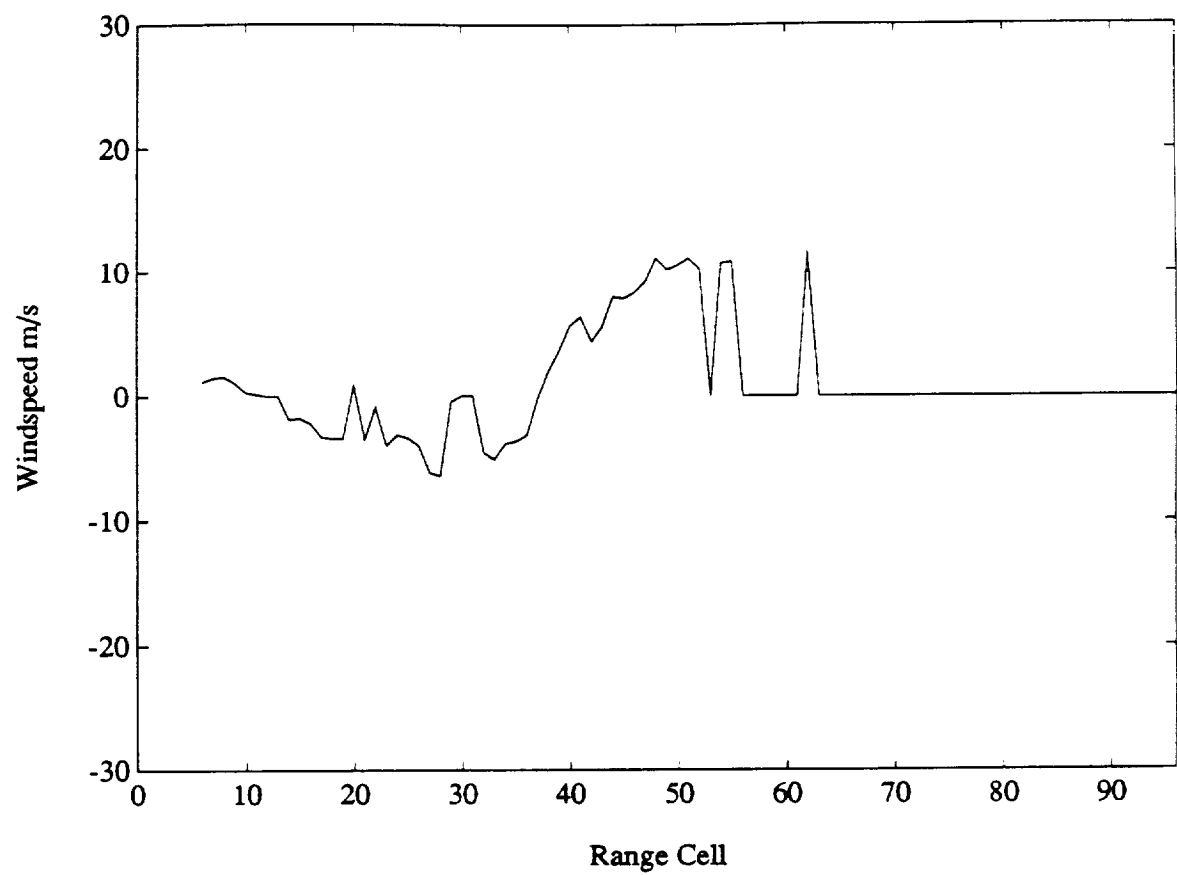


Figure 1.2 "S"-curve Pattern of a Typical Microburst

Computing the potential rate of climb assuming energy loss is negligible yields

$$\dot{h}_p = \frac{\dot{E}}{mg} = \frac{\nu \dot{\nu}}{g} + \dot{h} \quad (1.3)$$

which, when combined with aircraft equations of motion results in

$$\dot{h}_p = \frac{\dot{E}}{mg} = \frac{T - D}{mg} - \left[\frac{\dot{W}_x}{g} \cos \gamma + \frac{\dot{W}_h}{g} \sin \gamma - \frac{W_h}{\nu} \right] \nu \quad (1.4)$$

where T is aircraft thrust, D is drag, γ is the flight-path angle, and W_x and W_h are the horizontal and vertical components of the wind velocity. Assuming nearly stable flight, i.e., $T \approx D$ and $\gamma \approx 0$, equation (1.4) reduces to the hazard factor or “F-factor” equation

$$F = \frac{\dot{W}_x}{g} - \frac{W_h}{\nu} . \quad (1.5)$$

Equation (1.4) now becomes

$$\dot{h}_p = \frac{\dot{E}}{mg} = \frac{T - D}{mg} - F \nu . \quad (1.6)$$

Equation (1.6) defines quantitatively the performance decrease that a windshear condition may inflict upon an aircraft. Note that the “F-factor” in this equation is derived solely from windfield information, providing an aircraft-independent measure of the severity of the windfield. The thrust-to-weight ratio for any type of aircraft is then factored in to provide an aircraft specific hazard index. One common measure of hazard is defined for “F-factor” values above a typical threshold of 0.15.

1.4 Hazard Factor Algorithm

A method is presented in [5] for computing a hazard factor from windspeed estimates based on a weighted least-squares technique that reduces the effect of noise due to stationary and moving ground clutter. This hazard factor algorithm is currently implemented in the Airborne Windshear Doppler Radar Simulation (AWDRS) program [6] in addition to all hazard factor computations presented in this thesis. The technique estimates the slope of a linear function of windspeed vs. range for a given

range. Each windspeed measurement is weighted by the spectral width of the energy return, providing an estimate of the confidence of the measurement. Currently, windspeed estimates from five adjacent range cells are used for each computation of hazard. An advantage to the weighted least-squares algorithm is the addition of a measure giving the error of the estimate. This error is the averaged sum of the least-square residuals and can be used to identify wide cell-to-cell variations in windspeed estimates. Consider the measured windspeed, \hat{v}_j over m range cells ($m \approx 5$).

$$\hat{v}_j = b_1 + b_2 r_j + e_j \quad (1.7)$$

where b_1 and b_2 are constants, \hat{v}_j is the estimated mean Doppler velocity at range r_j , and e_j is the least-squares approximation error. The estimate b_2 represents the velocity-to-range slope and is desired for the estimate of hazard. Begin the least-squares solution for b_2 by representing (1.7) in matrix form

$$\bar{v} = A\bar{b} + \bar{e} \quad (1.8)$$

where \bar{v} is an $m \times 1$ column vector containing values of \hat{v}_j , \bar{b} is a 2×1 column vector containing b_1 and b_2 respectively, \bar{e} is the column vector of e_j values, and A is an $m \times 2$ matrix of the form

$$A = \begin{bmatrix} 1 & r_1 \\ 1 & r_2 \\ \cdot & \cdot \\ \cdot & \cdot \\ 1 & r_m \end{bmatrix}. \quad (1.9)$$

By adding a weighting matrix to the least-squares solution of 1.8, the estimates of \hat{v}_j with the greatest confidence level will influence the least-squares solution more, and the estimates which have a low confidence level will not influence the solution of (1.8) as much. The weighting matrix Φ is composed of spectral width measurements σ_j , producing

$$\Phi = \begin{bmatrix} \frac{1}{\sigma_1^2} & 0 & \cdot & \cdot & \cdot \\ 0 & \frac{1}{\sigma_2^2} & \cdot & \cdot & \cdot \\ \cdot & \cdot & \cdot & \cdot & \cdot \\ \cdot & \cdot & \cdot & \cdot & \cdot \\ \cdot & \cdot & \cdot & \cdot & \frac{1}{\sigma_m^2} \end{bmatrix}. \quad (1.10)$$

A discussion of spectral width estimators follows in Chapter 2. The weighting matrix is included into the least-squares pseudoinverse solution of (1.8) for matrix \bar{b} [7]

$$\bar{b} = (A^T \Phi^{-1} A)^{-1} A^T \Phi^{-1} \bar{v} . \quad (1.11)$$

From (1.11) the hazard level is contained in the b_2 component of matrix \bar{b} . Smoothing of this estimate over adjacent range cells through averaging is possible, although results presented in this thesis are without averaging. The error estimate or “goodness of fit” is equal to the weighted sum of the error vector \bar{e}

$$r = \frac{1}{m} [\bar{e}^T \Phi^{-1} \bar{e}] \quad (1.12)$$

and can be used to exclude an estimate as invalid if r is greater than a given threshold, indicating that the least-squares fit has substantial error.

1.5 Doppler Weather Radar

The advantage of pulse Doppler radar over conventional radar is Doppler’s ability to identify not only range to an object in the radar’s scanning area but also the relative velocities of these objects. For this reason, Doppler weather radar may prove to be an effective device in the detection and avoidance of hazardous low-altitude windshear by identifying approaching windfield characteristics. The ranging capability of the radar is achieved by measuring the time in which a transmitted pulse of energy is reflected off objects and returned to the receiver. The operating characteristics of Doppler radar from a time domain perspective have been thoroughly presented [8, 9, 10]. Here a frequency spectrum analysis of Doppler Radar is provided.

Scatterers which return transmitted radar energy will induce a Doppler shift in the frequency of the transmitted pulse energy proportional to the radial velocity between the object and the transmitting/receiving antenna. Objects approaching the antenna will cause a Doppler shift of the transmitted energy to a higher frequency while a diverging object relative to the antenna will create a Doppler shift to a lower

frequency. Consider a transmitted pulse, $s(t)$, having amplitude A which is composed of a single frequency, f_o ,

$$s(t) = A \cos(2\pi f_o t) \quad (1.13)$$

which has the following frequency spectrum:

$$S(f) = \mathcal{F}[s(t)] = \frac{1}{2} A e^{j(2\pi f_o t + \phi)} + \frac{1}{2} A e^{-j(2\pi f_o t + \phi)} \quad (1.14)$$

The amount of transmitted energy returned to the receiving antenna is equal to the sum of the return energy from all scatterers. The frequency of the return from scatterer i , will be Doppler shifted by an amount proportional to the relative velocity between the receiver and the scatterer and the total Doppler spectrum will be a distribution of returns from all scatterers. The relationship between the radial velocities of the scatterers and the corresponding shift in Doppler frequency can be shown through the Doppler equation for light as predicted by the theory of relativity [11]

$$f' = f \frac{1 - \frac{u}{c}}{\sqrt{1 - \left(\frac{u}{c}\right)^2}} \quad (1.15)$$

where f is the transmitted frequency and f' is the frequency observed by an object where the relative velocity between the source and the target is u and c is the speed of light. Negative u indicates that the objects are converging and positive u indicates that the objects are diverging. In the case of Doppler radar, the Doppler shift must be computed twice: first when the transmitted pulse reaches a scatterer, and again when the returned energy reaches the radar antenna. At the scatterer, the Doppler shift of the transmitted pulse can be described by

$$f'_i = f_o \frac{1 - \frac{v_i - v_a}{c}}{\sqrt{1 - \left(\frac{v_i - v_a}{c}\right)^2}} \quad (1.16)$$

where f'_i is the frequency observed at scatterer i , and v_i and v_a are the radial velocities of scatterer i and the aircraft, respectively. The aircraft velocity is included in order to remove the effect of a moving radar platform. The next step is to compute the

Doppler shift between the reflected energy, f'_i , and the frequency observed at the receiver, namely,

$$f_i = f'_i \frac{1 - \frac{v_i - v_a}{c}}{\sqrt{1 - \left(\frac{v_i - v_a}{c}\right)^2}}. \quad (1.17)$$

Combining (1.16) and (1.17) yields the total Doppler shift in terms of transmitted frequency and received frequency

$$f_i = f_o \left[\frac{1 - \frac{2(v_i - v_a)}{c} + \frac{(v_i - v_a)^2}{c^2}}{\sqrt{1 - \left(\frac{v_i - v_a}{c}\right)^2}} \right]. \quad (1.18)$$

Assuming $v_i - v_a \ll c$ allows for the elimination of second order terms, thus reducing (1.18) to the linear approximation

$$f_i = f_o \left[1 - \frac{2(v_i - v_a)}{c} \right]. \quad (1.19)$$

Equation (1.19) describes the relationship between the radial velocities of an airborne Doppler radar system and scatterers in its range cell volume and the Doppler shift in frequency of the returned signal. Assuming a transmitted pulse having the energy spectrum given in (1.14), the spectrum of the returned energy is

$$S_{ret}(f) = \sum_i \left\{ \frac{1}{2} A_i e^{j(2\pi f_i t + \phi_i)} + \frac{1}{2} A_i e^{-j(2\pi f_i t - \phi_i)} \right\} \quad (1.20)$$

where A_i is the amount of energy returned from scatterer i and ϕ_i is the phase offset due to scatterer i . Because the returned energy contains Doppler shifts about $\pm f_o$, it is necessary to demodulate the transmitted signal in order to obtain Doppler frequency shifts that are centered about zero frequency, as in stationary objects, rather than the transmitted frequency f_o . This demodulation is accomplished by multiplying the returned signal, S_{ret} by the single-sided complex exponential at frequency $f_s = f_o(1 + 2v_a/c)$, resulting in a negative shift in all frequencies of S_{ret} by f_s . Note that the modulation term f_s includes the aircraft velocity, which must be known. The shifted signal becomes

$$S_{IQ}(f) = S_{ret}(f) * \delta(f - f_s) \quad (1.21)$$

$$= \sum_i \left\{ \frac{1}{2} A_i e^{j(2\pi [f_i - f_s] t + \phi_i)} + \frac{1}{2} A_i e^{-j(2\pi [f_i + f_s] t - \phi_i)} \right\}. \quad (1.22)$$

Applying (1.19) and the formula for the wavelength of an electromagnetic signal, $\lambda_o = c/f_o$, to (1.22) yields

$$S_{IQ}(f) = \sum_i \left\{ \frac{1}{2} A_i e^{j(2\pi[-\frac{2v_i}{\lambda_o}]t + \phi_i)} + \frac{1}{2} A_i e^{-j(2\pi[2f_s - \frac{2v_i}{\lambda_o}]t + \phi_i)} \right\}. \quad (1.23)$$

The second term in (1.23) can be removed through a low-pass filter resulting in a complex baseband signal representing the returned Doppler shift centered about zero frequency. This signal is commonly represented by its resulting in-phase and quadrature-phase time series returns of the form

$$I = \sum_i \left[A_i \cos \left(\frac{-4\pi v_i}{\lambda_o} t + \phi_i \right) \right] \quad (1.24)$$

$$Q = \sum_i \left[A_i \sin \left(\frac{-4\pi v_i}{\lambda_o} t + \phi_i \right) \right]. \quad (1.25)$$

Equations (1.24) and (1.25) define the complex time series referred to as IQ data in terms of the sum of Doppler shifts caused by all scatterers. I refers to the real component of the complex series while Q refers to the imaginary component. For any single scatterer, the complex frequency of the IQ data will be related to the line-of-sight velocity of the scatterer relative to ground, that is,

$$f_{dopp} = -\frac{2v}{\lambda_o} \quad (1.26)$$

where v is the ground velocity of the scatterer projected along the line-of-sight from the radar antenna to the scatterer. For a given sampling rate equal to the pulse-repetition frequency (PRF), the greatest unaliased frequency returned is

$$f_{max} = \frac{1}{2T_s} \quad (1.27)$$

and the maximum unambiguous velocity of a scatterer is

$$v_{max} = \frac{\lambda_o}{4T_s}. \quad (1.28)$$

The radar parameters used for all analysis include a PRF of 3755 pulses-per-second, a pulse width of $0.96\mu s$, and a transmitted frequency of 9.33625 GHz ($\lambda_o = 3.21103$ cm). From (1.28) the maximum unambiguous relative velocity for this situation will be equal to 30.14 m/s.

1.6 Problem Statement

The ability to detect a hazardous condition with the “F-factor” index relies heavily upon the accuracy of the windspeed estimates obtained. Strong clutter returns can heavily bias pulse-pair and spectral mean estimates of windspeed. A common approach to increasing the signal-to-clutter ratio for better windspeed estimation is to implement a notch filter to reduce the main clutter return which is usually present near zero relative velocity. This filtering can, however, attenuate the weather return which will further reduce the accuracy of the windspeed estimate. Proposed is a method whereby an unbiased estimate of windspeed can be achieved in a computationally attractive procedure and without clutter rejection filtering.

CHAPTER 2

WINDSPEED ESTIMATION

Although a Doppler weather radar system cannot directly measure windfield conditions, it is possible to infer information about such conditions when the radar return is a backscattering of energy from targets which are suspended particles and whose motion is controlled by the prevailing windfield conditions. As shown in section 1.5, the returned radar energy for a given volume will consist of a collection of returns from all targets that scatter or reflect the incident radar energy. In the case of a Doppler weather radar system, the targets are assumed to be particles suspended in the resolution volume, such as rain droplets, dust, or insects. From the Doppler spectrum, which contains a distribution of returns from all targets, windspeed estimation techniques attempt to characterize the windfield motion in the current resolution volume based on the motion of the targets in the resolution volume.

2.1 Time Domain Pulse-Pair Mean and Width Estimator

The time domain pulse-pair processor is a mean frequency estimator that provides an estimate of Doppler spectral mean and width in terms of the first autocorrelation lag. The pulse-pair Doppler mean estimate is [12]

$$\hat{v} = \frac{-\lambda_0}{4\pi T_s} \arg\{\hat{R}(T_s)\}, \quad (2.1)$$

with the autocorrelation of the time series at lag T_s given by

$$\hat{R}(T_s) = \frac{1}{N} \sum_{n=0}^{N-2} x^*(n) x(n+1). \quad (2.2)$$

Let $x(n)$ be a series of N complex IQ data samples recorded at the pulse repetition interval, T_s , where $T_s = 1/PRF$. Equation (2.2) is then equal to the complex autocorrelation of $x(n)$ at a lag of one pulse, thus, define $\hat{R}_1 = \hat{R}(T_s)$. The corresponding

pulse-pair Doppler width estimate for $x(n)$ is

$$\hat{\sigma}_v = \frac{\lambda}{2\pi T_s \sqrt{2}} \left| \ln \left(\frac{\hat{S}}{|\hat{R}_1|} \right) \right|^{1/2} \text{sgn} \left[\ln \left(\frac{\hat{S}}{|\hat{R}_1|} \right) \right] . \quad (2.3)$$

In (2.3), \hat{S} is the total power in the data sequence,

$$\hat{S} = \frac{1}{N} \sum_{n=0}^{N-1} |x(n)|^2 . \quad (2.4)$$

The sgn term is included in order to tag the width estimate with a negative value on the occasion when the estimate $\hat{R}(T_s)$ is greater than the estimate \hat{S} . For the case where $\hat{\sigma}_v \ll 1$, an alternate width estimator [12] can be used

$$\hat{\sigma}_v = \frac{\lambda}{2\pi T_s \sqrt{2}} \left| 1 - \frac{|\hat{R}_1|}{\hat{S}} \right|^{1/2} \text{sgn} \left(1 - \frac{|\hat{R}_1|}{\hat{S}} \right) . \quad (2.5)$$

This estimate of spectral width is only valid over the given range of narrow widths due to a bias present at larger spectral widths.

2.2 Frequency Domain Pulse-Pair Mean and Width Estimator

The frequency domain pulse-pair mean estimator performs a similar analysis with similar results as its time domain counterpart. The difference is that the frequency domain estimator computes the autocorrelation of the sequence at lag T_s from the power spectrum rather than from the time series. The equation for Doppler mean estimate remains the same as in (2.1), that is,

$$\hat{v} = \frac{-\lambda_0}{4\pi T_s} \arg \hat{R}(T_s) . \quad (2.6)$$

However, the first autocorrelation lag can be derived directly from the power spectrum with

$$\hat{R}_1 = \frac{1}{N} \sum_{k=0}^{N-1} W(k) e^{j \frac{2\pi k}{N}} \quad (2.7)$$

where the power spectrum is defined as

$$W(k) = |X(k)|^2 = \left| \sum_{n=0}^{N-1} x(n) e^{-j \frac{2\pi n k}{N}} \right|^2 . \quad (2.8)$$

In order for the autocorrelation of (2.7) to yield the same results as (2.1) at least one zero must be appended to the time series $x(n)$ before the discrete fourier transform (DFT) is implemented to give $X(k)$. This is due to the nature of the DFT, which assumes a periodic time series. Without a padding of at least one zero value, the inverse DFT implementation of (2.7) would correlate the last sample $x(N-1)$ with the first sample $x(0)$. The frequency domain spectral width estimator resembles the corresponding time domain width estimator given in (2.3) and (2.5) except for the modified autocorrelation estimate \hat{R}_1 and the total power estimate \hat{S} . The total power is equal to the sum of the power spectrum

$$\hat{S} = \frac{1}{N} \sum_{k=0}^{N-1} W(k) . \quad (2.9)$$

The computation of pulse-pair spectral mean and width in either the time domain or the spectral domain yield similar results. Therefore, the implementation of one technique over the other would normally be based on computational costs.

2.3 Spectral Domain Mean-Variance Mean and Width Estimator

An alternative algorithm estimates the Doppler mean and width by computing the mean and variance of the given power spectrum directly in the spectral domain. For this algorithm, the first and second moments about an estimate mean bin number, k_m , are computed [12]. k_m is determined from the frequency bin in $W(k)$ containing maximum energy. The Doppler mean estimate is then computed with

$$\hat{v} = \frac{-\lambda}{2N} \left\{ \frac{k_m}{T_s} + \frac{1}{\hat{S} T_s} \sum_{k=k_m-\frac{N}{2}}^{k=k_m+\frac{N}{2}} (k - k_m) W[\text{mod}_N(k)] \right\} . \quad (2.10)$$

In (2.10), \hat{S} is the total power of the data sequence and $\text{mod}_N(k)$ denotes k modulo N . The Doppler width estimate $\hat{\sigma}_v$ is equal to the variance of the power spectrum about k_m ,

$$\hat{\sigma}_v = \left[\frac{\lambda^2}{4\hat{S}T_s^2} \sum_{k=k_m-\frac{N}{2}}^{k=k_m+\frac{N}{2}} \left(\frac{k}{N} + \frac{2\hat{v}T_s}{\lambda} \right)^2 W[\text{mod}_N(k)] \right]^{1/2} . \quad (2.11)$$

2.4 The Effect of Clutter on Windspeed Estimates

A major concern with airborne pulse Doppler radar systems is the presence of strong energy returns from targets not controlled by wind. These targets can be stationary or moving objects on the ground, or objects in the range cell volume whose motion is not controlled by the wind such as birds or other aircraft. In situations involving heavy rainfall, it has been observed that the main rain shaft may not be under the control of divergent winds and may appear as a mode about Doppler zero, similar to a ground clutter signature. Unwanted returns originating from the ground are called ground clutter and can significantly inhibit a system's ability to correctly identify a hazardous condition. Due to physical requirements which necessitate the use of antenna elevation angles directed at or near the ground, airborne weather radar systems are more susceptible to the effects of ground clutter contamination than ground based systems with much higher antenna elevations.

Although microburst conditions can occur at any altitude, it is the low-altitude windshear events which inherently pose the greatest hazard to an aircraft penetrating such an event due to the horizontal shear created by the microburst as it impacts the ground. This hazard is also complicated by the low altitude of the scenario which provides the pilot with a relatively short response time in which to avoid catastrophe. In order for an airborne radar system to observe such low-altitude events, antenna elevation angles must be kept small so that any hazardous windshear conditions can be identified. Antenna elevations currently being used are typically within three degrees above or below horizontal. At these elevations, radar return from antenna sidelobes can introduce much unwanted clutter into the received signal, especially at closer ranges.

Moving objects on the ground such as cars on a nearby interstate highway can create "discrete clutter" which will appear as a narrow spectral peak within the returned IQ data. This form of clutter can impair the ability to correctly estimate

windspeed values because the clutter can be located anywhere in the Doppler spectrum and thus, is difficult to characterize. The implications of discrete clutter on modal analysis are discussed in Chapter 4.

Because clutter from stationary reflectors can be characterized as a spectral mode near Doppler zero, it can be more readily removed through a clutter rejection filter. The presence of a strong clutter return can severely impair the ability of mean spectral estimators such as pulse-pair and mean-variance to correctly identify the windspeed conditions present in a given range cell. Clutter can bias a windspeed estimate toward Doppler zero or in the event of a strong clutter return and a weak weather return, completely cover the weather return signature. However, by identifying clutter characteristics, measures can be taken to reduce the unwanted effects of clutter upon windspeed estimators.

2.5 Clutter Rejection Filters

The general approach to reducing the effect of clutter on windspeed estimates is to remove the clutter return through filtering. Several types of clutter rejection filters exist which can improve the quality of mean spectral estimators by attempting to remove returns from clutter targets while retaining returns from weather targets. Because weather and clutter returns may overlap both spatially and temporally, a complete removal of clutter return energy without some attenuation to any weather return present is not possible. In general, clutter energy is characterized as a narrow band near Doppler zero. Clutter rejection filters are typically notch filters which remove spectral energy near Doppler zero. Some typical clutter rejection filtering methods include (1) finite impulse response (FIR) notch filter [13, 14, 15], (2) infinite impulse response (IIR) notch filter [13, 14, 15], and (3) spectral domain line editing (ideal notch filtering) [13]. The disadvantages to clutter rejection filtering are the additional computational resources needed and the possible attenuation of the weather signal below a detectable level.

CHAPTER 3

SPECTRAL ESTIMATION USING MODAL ANALYSIS

Typically, mean estimators such as the pulse-pair method function by attempting to reduce the energy return through filtering so that the remaining return appears to have originated from a single source.

Proposed is a method for windspeed estimation based on a modal analysis approach which would not require filtering of an unwanted clutter return. Unlike the pulse-pair estimator, a modal analysis approach attempts to model the returns from all sources. In this way, it attempts to identify all dominant sources of energy return present without having to rely on a single mean estimator for the windspeed such as the pulse-pair estimator, which can only yield a single spectral location parameter associated with the return data. When the spectral content of the return data includes more than one mode, the single pulse-pair estimate will attempt to reflect both modes with a single value producing an estimate that is potentially uncharacteristic of either mode. To compensate for this, clutter rejection filtering generally is used in conjunction with the pulse pair-estimator. Filtering attempts to remove the return energy from undesired sources while retaining the return energy from the desired weather source. In contrast, a modal approach to windspeed estimation models the return energy from all sources and then attempts to classify the source of each return.

For the problem at hand, the primary sources of return energy to the Doppler radar system are weather and clutter. Based on the assumption that only these two primary sources of return energy exist, a method of spectral estimation which involves the modeling of two dominant modes is sufficient. Once the identification of the spectral modes is achieved, a statistical two-class pattern recognition routine can be employed for the classification of modes.

3.1 The Prony Approach

The Prony method was created by Gaspard Riche, Baron de Prony as a means of representing the expansion of various gases in terms of the sums of complex exponentials. Assume that there exists a sequence, x_n , consisting of N complex data samples. The Prony method generates an alternate series, \hat{x}_n , which approximates the original series through a summation of M complex exponential terms [16, 17]. For an approximation where $N \leq 2M$, the exact series can be represented and \hat{x}_n will equal x_n . For situations where $N > 2M$, an approximation of x_n containing some error will be generated. Define the approximation

$$\hat{x}_n = \sum_{m=1}^M C_m \mu_m^n, \quad \text{for } n = 0, \dots, N-1 \quad (3.1)$$

where C_m and μ_m are complex values of the form

$$C_m = A_m \exp j\theta_m \quad (3.2)$$

$$\mu_m = \exp [(\alpha_m + j2\pi f_m)\Delta t] . \quad (3.3)$$

Equations (3.2) and (3.3) consist of four parameters. A_m is amplitude, θ_m is initial phase, α_m is a damping factor, and f_m is frequency in Hertz. The N equations in (3.1) contain the $2M$ complex unknowns C_m and μ_m for $1 \leq m \leq M$. Prony's technique provides a method of solving for the parameters $\{A_m, \theta_m, \alpha_m, f_m\}$ that will minimize the squared error

$$\varepsilon = \sum_{n=0}^{N-1} |\epsilon_n|^2 \quad (3.4)$$

where the approximation error is the difference between the measured series and the estimated series

$$\epsilon_n = x_n - \hat{x}_n . \quad (3.5)$$

To begin the Prony approach, define the equation

$$\sum_{m=0}^M a_m \mu^{M-m} = \prod_{m=1}^M (\mu - \mu_m), \quad a_0 = 1 \quad (3.6)$$

so that the values of μ_m in (3.1) correspond to the roots of equation (3.6). Next, multiply (3.1) by a_p and substitute $(n - p)$ for n so that

$$\hat{x}_{n-p} a_p = \sum_{m=1}^M C_m a_p \mu_m^{n-p} \quad (3.7)$$

for $0 \leq n - p \leq N - 1$. Next, replace μ_m^{n-p} with $\mu_m^{n-M} \mu_m^{M-p}$ to get

$$\hat{x}_{n-p} a_p = \sum_{m=1}^M C_m a_p \mu_m^{n-M} \mu_m^{M-p} . \quad (3.8)$$

After the summation of both sides of (3.8) over $0 \leq p \leq M$ note that the final summation of

$$\sum_{p=0}^M \hat{x}_{n-p} a_p = \sum_{m=1}^M C_m \mu_m^{n-M} \sum_{p=0}^M a_p \mu_m^{M-p} = 0 \quad (3.9)$$

is of the form of (3.6) evaluated at one of its roots and thus, equals zero. The left side of (3.9) will form the recursive difference equation

$$\hat{x}_n = - \sum_{m=1}^M a_m \hat{x}_{n-m} \quad (3.10)$$

defined over $m \leq n \leq N - 1$. Note that (3.10) is in terms of the approximation series \hat{x} which is still undetermined. By including the approximation error e from (3.5), the difference equation of (3.10) can be expressed in terms of the original series x_n . Substituting for the approximation series in (3.10) results in

$$x_n = - \sum_{m=1}^M a_m \hat{x}_{n-m} + e_n \quad (3.11)$$

$$= - \sum_{m=1}^M a_m x_{n-m} + \sum_{m=0}^M a_m e_{n-m} \quad (3.12)$$

defined for $M \leq n \leq N - 1$. The Prony method requires the solution of (3.12) for the a 's while minimizing the squared error e_n . An iterative solution to this difficult nonlinear system has been presented by Huggins and McDonough [18].

3.2 Extended Prony Analysis

The extended Prony technique is a method whereby the nonlinear characteristics of (3.1) can be linearized at the cost of an acceptable, yet sub-optimal solution [16]. The error measure for the Prony technique has been shown to be the difference between the sampled data x_n and a linear prediction series based on M previous samples of the approximation series. To simplify (3.11) into a linear equation where the values a_m can be determined efficiently, define a modified error measure equal to the difference between x_n and a linear prediction series based on M previous samples $\{x_{n-M}, x_{n-M+1}, \dots, x_{n-1}\}$,

$$x_n = - \sum_{m=1}^M a_m x_{n-m} + \epsilon_n \quad (3.13)$$

where the modified error is

$$\epsilon_n = \sum_{m=0}^M a_m e_{n-m} . \quad (3.14)$$

By minimizing this revised error measure, (3.13) degenerates into an efficient spectral estimation technique known as Autoregressive (AR) parameter estimation. Appendix A describes AR modeling and presents an efficient method for AR parameter estimation.

3.3 Second Order Extended Prony Analysis

Presented in this section is an implementation of a second order extended Prony technique applied to windspeed estimation of pulse Doppler weather radar data. The extended Prony approach begins with any AR parameter estimation technique which will generate the second order coefficients a_1 and a_2 . The Levinson-Durbin algorithm described in Appendix A will be used to generate the AR coefficients due to its low computational requirements which would facilitate implementation on a real time windshear detection system. From the AR coefficients a_1 and a_2 the values of μ_1 and μ_2 from (3.1) are determined through rooting the characteristic polynomial

$$\mu^2 + a_1\mu + a_2 = 0 . \quad (3.15)$$

Note that μ_1 and μ_2 are the pole locations in the z -plane of the AR process. For the second order case, these pole locations can be solved by way of the quadratic equation

$$\mu_+ = \frac{-a_1 + \sqrt{a_1^2 - 4a_2}}{2} \quad (3.16)$$

$$\mu_- = \frac{-a_1 - \sqrt{a_1^2 - 4a_2}}{2} . \quad (3.17)$$

The desired frequency estimates as well as damping factors are derived from the values of μ_+ and μ_- . The parameters C_1 and C_2 contain information about amplitude and phase of the Prony model, but are not required for an extended Prony analysis. Recalling that the μ 's are related to the frequency estimates by $\mu_m = \exp[(\alpha_m + j2\pi f_m)\Delta t]$ and that Δt is equal to the inter-pulse period T_s , the frequency values f_1 and f_2 are computed with

$$f_i = \frac{1}{2\pi T_s} \arg(\mu_i) . \quad (3.18)$$

The desired windspeed estimated can now be inferred from the conversion from frequency to velocity

$$v_i = \frac{-\lambda_o f_i}{2} = \frac{-\lambda_o}{4\pi T_s} \arg(\mu_i) . \quad (3.19)$$

Note the similarity between (3.19) and the pulse-pair equation given in (2.1). In fact, the pulse-pair estimate of Doppler velocity is analogous to a windspeed estimate from a first order AR model where the argument term would be the coefficient a_1 .

For reasons to be made clear in Chapter 4, a different assignment of the two poles will be defined according to the magnitude of the respective Doppler velocities. That is for pole 1

$$\mu_1 = \begin{cases} \mu_+, & |v_+| \geq |v_-| \\ \mu_-, & \text{else} \end{cases} \quad (3.20)$$

and for pole 2

$$\mu_2 = \begin{cases} \mu_+, & |v_-| > |v_+| \\ \mu_-, & \text{else} \end{cases} . \quad (3.21)$$

The damping factors α_1 and α_2 yield information about the spread of a spectral mode. Small damping factors indicate wide spectral modes while larger damping factors indicate narrower modes. The damping factors are equal to

$$\alpha_i = \frac{\ln |\mu_i|}{\text{PRF}} . \quad (3.22)$$

It has been stated that the extended Prony method can yield a greatly simplified, yet sub-optimal solution compared to the Prony technique. The concession made by the extended Prony method is that the damping factor, α_m , and amplitude, A_m , have been reduced to a single parameter. This parameter is directly related to both the damping factor and the amplitude of the spectral mode. A pole value with a magnitude near unity will have a relatively large magnitude and a relatively small damping factor, while a pole with a small magnitude will produce a smaller amplitude and a larger damping factor. When one factor is changed the other will be changed as well. This concession is not a concern in the present windshear detection problem as only amplitude, and not the damping factor, is used in the current analysis.

A comparison between a second order AR model spectral estimate and an FFT spectral estimate for a sample data set is provided in Figure 3.1. This 96 point IQ data set contains returns from two distinct spectral modes: one mode is centered about zero Doppler velocity while the other mode is at some negative velocity indicating motion in a direction toward the aircraft. For the FFT operation, the sample data has been zero-padded to a length of 128. Pole 1 and Pole 2 reflect the values of μ_1 and μ_2 converted into a polar form where the pole's magnitude and argument are represented. Note how the magnitude of each pole is reflected in the relative height of the spectral peaks and that each pole's argument converted to Doppler velocity through (3.19) corresponds to the Doppler velocity of the spectral modes and the local maxima in the AR spectral density. Even though a second order model such as the the example in Figure 3.1) cannot be expected to provide an accurate and

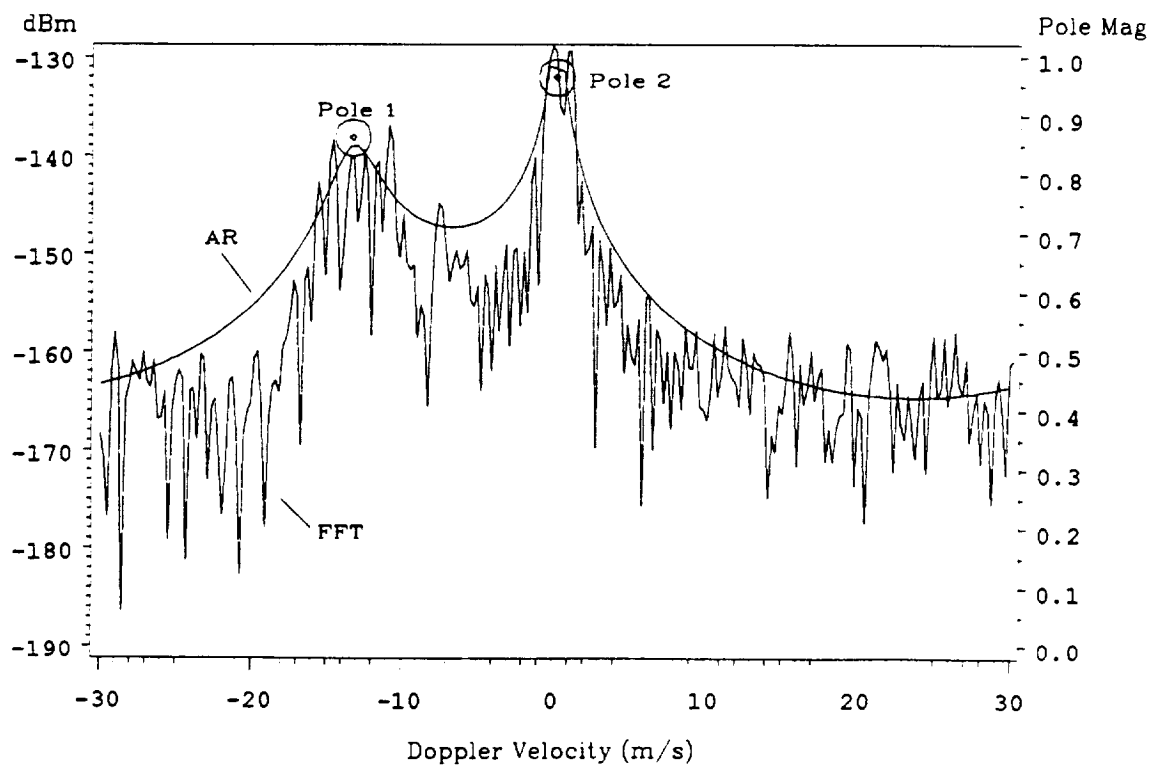


Figure 3.1 Second Order AR Spectral Estimate and Pole Locations

detailed spectral density, it is possible, however, for such a model to provide accurate estimates of the frequencies associated with dominant spectral modes.

It is now possible to combine the pole values from a single range cell, such as in Figure 3.1 with other pole values from all range cells in any given radar snapshot. Figure 3.2 is a bubble plot which represents a series of 91 range cells and the pole values which correspond to that cell. From the radar parameters given in section 1.5, each range cell represents approximately 145 meters. On the bubble plot each range cell has two circles associated with it which represents the argument and magnitude of the second order pole locations. Pole magnitudes, that is their distance from the z -domain origin, is shown by the size of the circles, while the argument of a pole is translated into its corresponding Doppler velocity estimate as computed by (3.19). When viewing the two velocity estimates associated with a second order extended Prony technique for the data in Figure 3.2, two distinct modes appear indicating that the energy in the return is from two or more separate return sources. In Figure 3.2 both a weather mode and a clutter mode are apparent. The “S”-curve feature can be classified as weather return from a microburst event [19] while the strong mode present throughout all range cells near Doppler zero can be classified as a clutter mode. In this example, range cells 65-96 contain both a strong central clutter mode as well as a weaker mode located near ± 30 m/s. The pole values for these range cells can be attributed to neither a weather nor a clutter return, but is a result of the AR modeling process which will be discussed further in Chapter 4.

The windspeed estimates of the weather mode can be considered to be an unbiased estimate because both spectral modes are modeled independently of each other. The clutter return should be reflected in the clutter mode, leaving the weather mode to reflect mostly weather return. For this reason, clutter rejection filtering is not required for windspeed estimation with this modal approach.

A complication to this second order approach arises due to the generation of two velocity estimates for each range cell volume, but the need of only a single windspeed

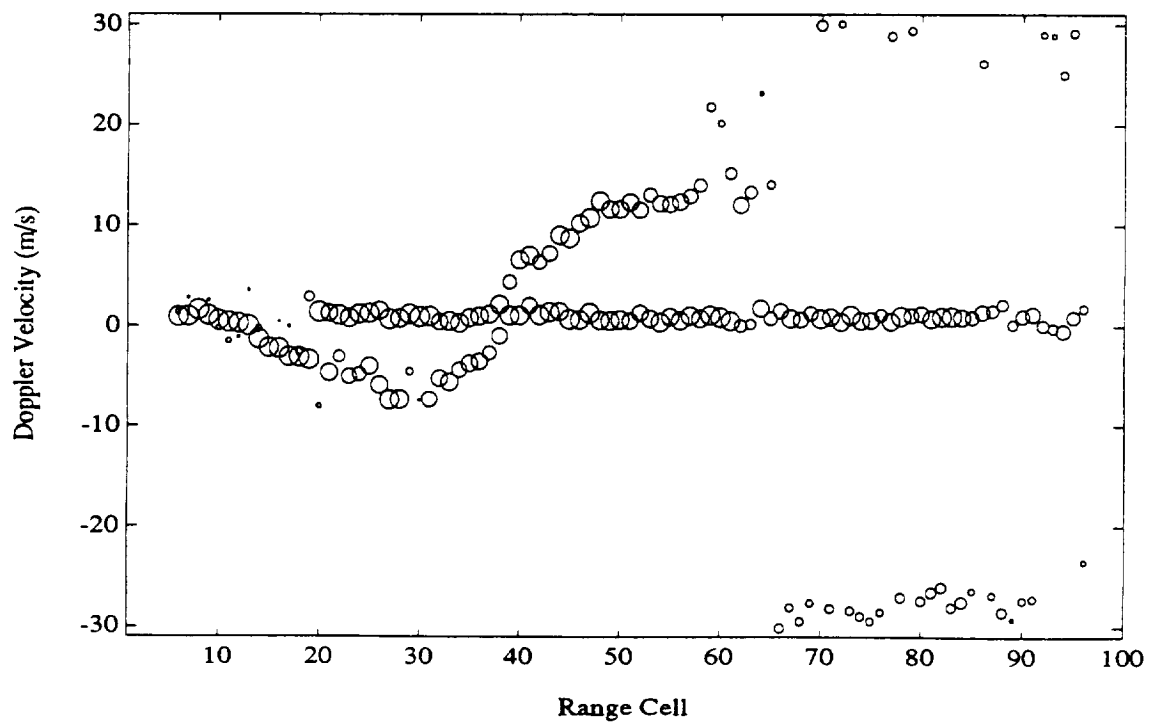


Figure 3.2 Bubble Plot of Velocity Estimates for a Microburst Event

estimate. Chapter 4 addresses this topic and presents various methods which attempt to resolve the problem of characterizing the windfield through a second order extended Prony approach.

CHAPTER 4

WINDSPEED ESTIMATION FROM A TWO POLE MODEL

As introduced in Chapter 3, a second order Prony model may avoid the need for typical clutter rejection filtering. However, further processing is required in order to formulate a valid windspeed estimate. The identification of two spectral modes by the extended Prony approach presented in Chapter 3 introduces the need for some form of classification which can distinguish those modes that identify clutter sources from those modes that identify weather sources. Presented in this chapter are two classification schemes which attempt to derive a windspeed estimate given the parameters of a second order Prony model. The first classification scheme forms a windspeed estimate based on the Doppler velocities associated with the poles of a second order all-pole model. The second scheme implements an approximation which allows for a windspeed estimate to be determined directly from the coefficients of a second order autoregressive (AR) model which reduces the computational load of the windspeed estimator.

4.1 Characterizing the Poles

Before attempting to classify spectral modes based on second order extended Prony method pole values, discriminating characteristics are needed which will exploit differences between clutter returns and weather returns. Such a statement assumes that dominant weather and clutter modes present in the Doppler spectra will be represented by a second order AR model. The complex pole values associated with such a model yield information about the Doppler velocity and relative intensity of the spectral modes through the pole's argument and magnitude, respectively. To examine how a second order model might represent weather and clutter characteristics, first analyze the Doppler spectrum over a series of range cells for situations with and

without a weather return present. A 20th order AR model is used in Figures 4.1 and 4.2 to provide a high order approximation of spectral density for each range cell in both a simulated dry microburst event (Figure 4.1) and a clutter only situation (Figure 4.2). Both situations simulate an aircraft on final approach to Denver Stapleton airport runway 26R with the microburst model D51. For each run the antenna azimuth was set at -10 degrees, antenna elevation was 1 degree above a glideslope of 3 degrees, and the aircraft was positioned 7.4 km from touchdown. All simulation parameters have been included in Appendix C. Data for the microburst model have been derived from data collected during an actual microburst event which occurred on July 11, 1988 at Stapleton airport [20]. In the dry microburst situation, the energy return from the leading edge of the outflow can be seen as a negative Doppler shift(headwind) with a peak Doppler velocity of about -14 m/s in the vicinity of range cell 22, while the backside of the outflow has a weaker return but can be distinguished as a positive Doppler shift in the following range cells. In comparison, the "clutter only" situation, shown in Figure 4.2 does not contain the "S"-curve pattern commonly described as characterizing a microburst event. Instead, the return with little or no weather appears as a single spectral mode near Doppler zero. To examine the pole values for both the weather plus clutter situation and the clutter only situation, bubble plots similar to Figure 3.2 in Chapter 3 are included in Figures 4.3 and 4.4. It can be observed that for the dry microburst situation (Figure 4.3), the front edge of the microburst is reflected by negatively shifted poles in range cells 20-28 while the weaker outflow shows up as positively shifted poles in range cells 30-46. For the clutter only situation (Figure 4.4), there appears to be no pole pattern which would indicate any return other than clutter. Range cells 6-22 each contain one strong pole near Doppler zero and one weaker pole near ± 30 m/s. These weaker poles (defined as pole 1 because they have the greater Doppler velocity) may at first appear to represent a weak weather mode since clutter is primarily near Doppler zero, but upon

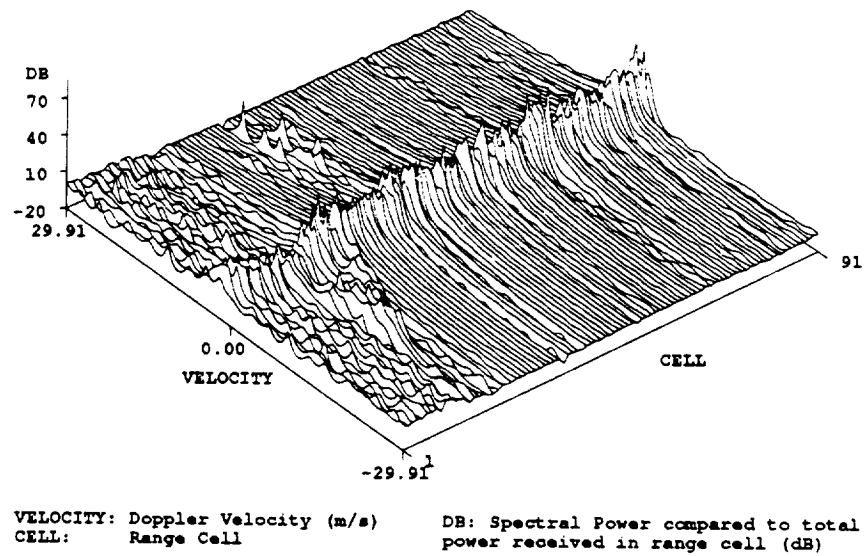


Figure 4.1 20th Order AR Spectra for a Simulated Microburst and Clutter Return

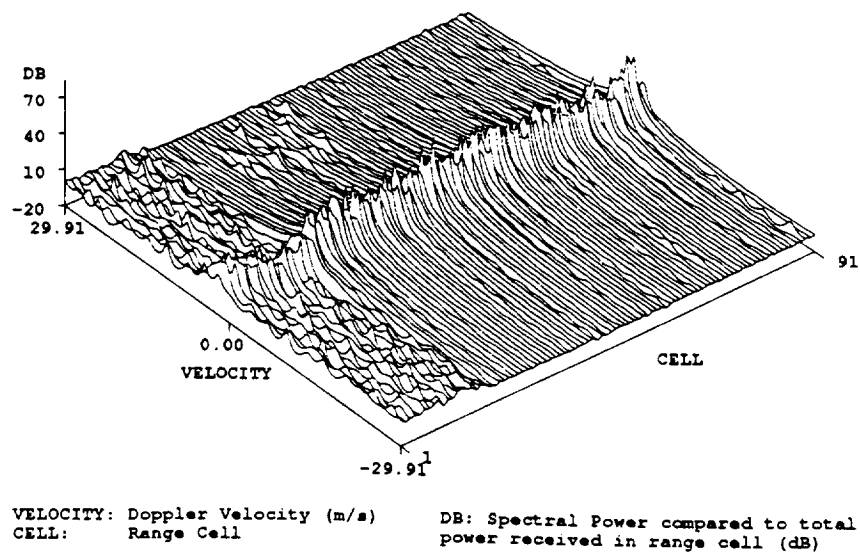


Figure 4.2 20th Order AR Spectra for a Simulated Clutter Only Return

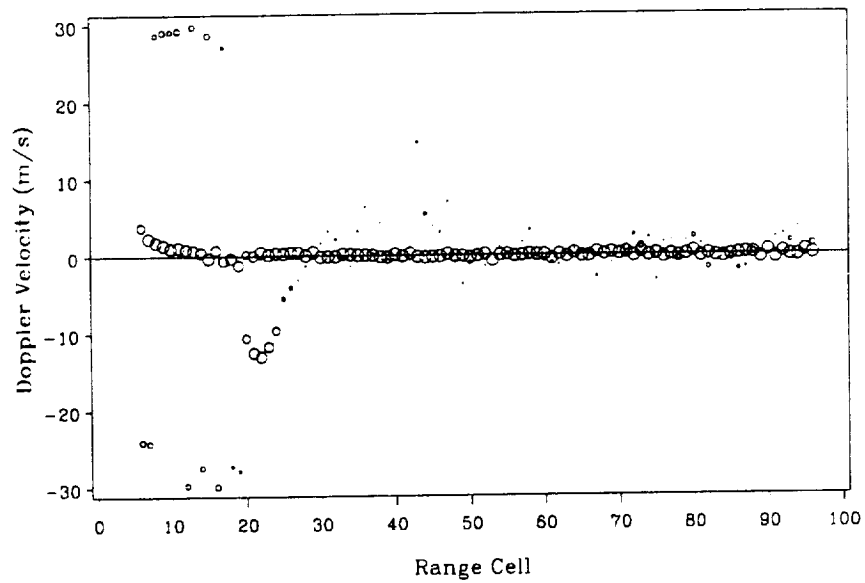


Figure 4.3 Bubble Plot for Simulated Microburst and Clutter Return

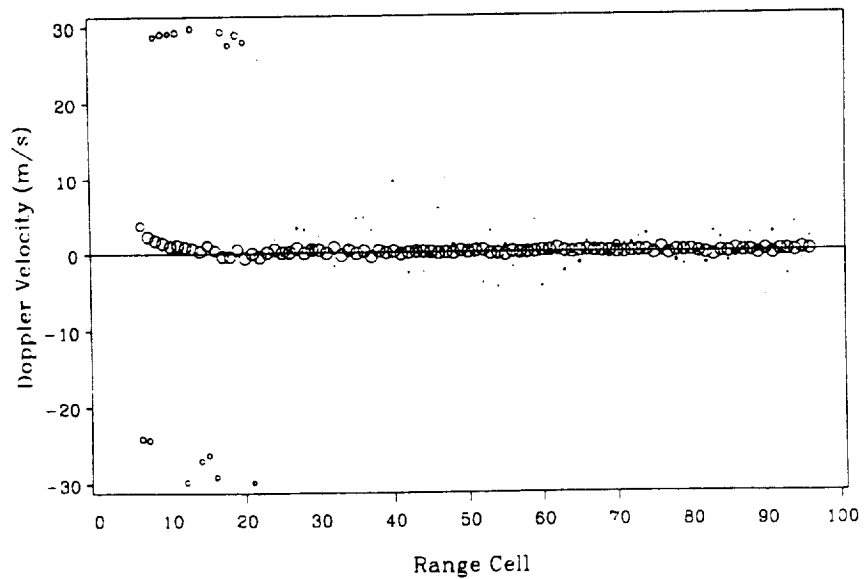


Figure 4.4 Bubble Plot for Simulated Clutter Only Return

inspection their presence can be attributed to a pole spreading effect resulting from the AR modeling process.

4.2 Pole Spreading Effect from AR Modeling

When the spectral content of a range cell is comprised primarily of a single strong clutter mode, the pole values computed with a second order extended Prony method will tend to double up to reflect this spectral mode. When the spectral content of the return is of a more even distribution, that is, no single spectral mode dominates the return, the poles will tend to spread out across the Doppler spectrum so that one pole is at the central clutter mode while the other pole is situated approximately half the distance around the unambiguous Doppler velocity spectrum.

This spreading effect is detrimental to the classification of weather poles and thus, windspeed estimation. Difficulties arise due to similarities between weather poles and poles resulting from a modeling effect when no weather return is present. Much of the effort to classify weather poles from non-weather poles is directed toward distinguishing and removing poles caused by spreading from valid weather poles.

The spreading out effect of the poles along the Doppler spectrum is not only limited to a second order model, but is also seen in higher order models as well. For example, Figure 4.5 is a bubble plot of the same clutter only simulation but with three poles per range cell. Observe that in range cells 6–22 the three pole values are distributed evenly throughout the Doppler spectrum, that is all poles are positioned approximately 20 m/s from the other two pole location in the Doppler velocity spectrum. These are the same range cells where pole spreading was observed in the two pole case. In the latter range cells, pole spreading occurs, but in this case, the central clutter mode is more dominant and attracts two pole values while only the third pole spreads away from the other two.

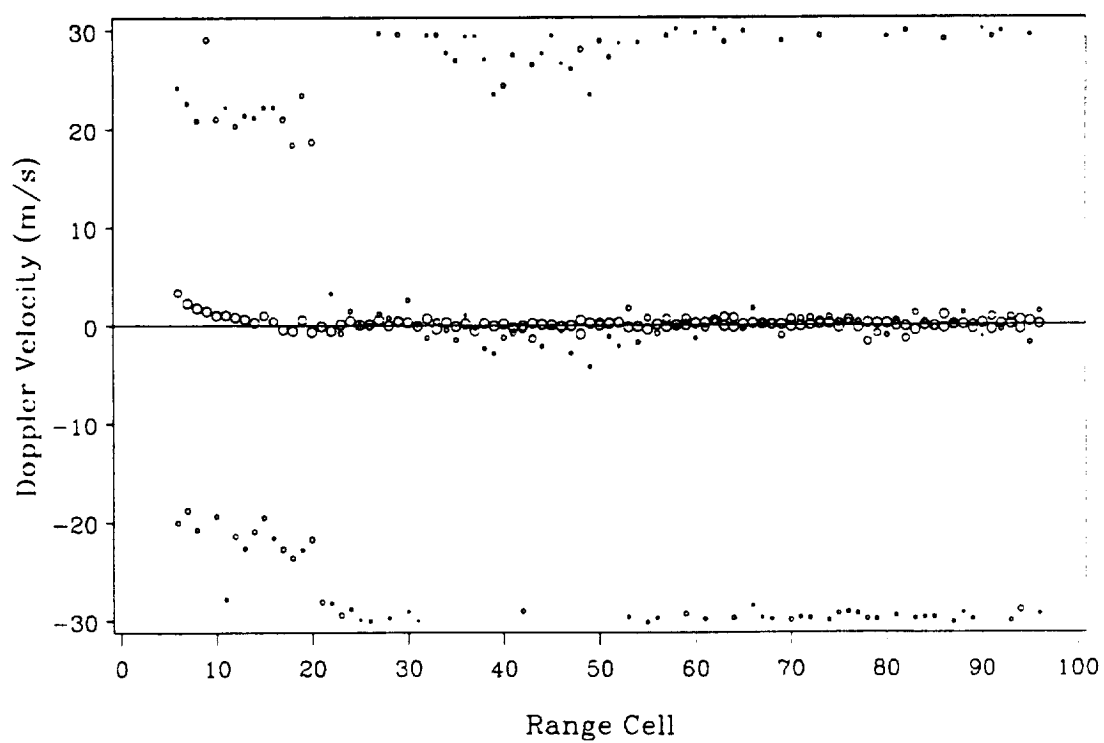


Figure 4.5 Bubble Plot for Third Order Simulated Clutter Only Return

4.3 Two Class Pattern Recognition Technique

In statistical pattern recognition terms, the second order extended Prony method sets up the basis for a two class pattern recognition problem [21] where the two classes of interest are weather and no weather. Since a windspeed estimate is actually the desired result, certain conditions will be incorporated into the classification system:

1. Pole 1 is defined as that pole with the greatest Doppler shift.
2. Pole 2 is defined as the remaining pole in each range cell.
3. Pole 1 may or may not be classified as weather.
4. Pole 2 will always be classified as non-weather.
5. Both poles may be classified as non-weather poles.
6. The windspeed estimate for a range cell with a pole classified as weather will be the Doppler velocity associated with the weather pole.
7. The windspeed estimate for a range cell without a pole classified as weather will be zero.

Condition 7 deserves further discussion. It states that if neither pole is given the classification of weather then the windspeed estimate will be assigned a zero value. For a return consisting of stationary clutter with pole spreading, or for a return with discrete clutter, a spectral mode away from zero will be present that is not a result of a weather return. A classification scene will attempt to distinguish between these non-weather pole sources and true weather sources in an effort to estimate windspeed. When pole 1 is away from Doppler zero and the classifier determines that it is not weather, then the windspeed estimate will be zero on the basis that no pole could be identified as a weather source.

At this point, the definition from Chapter 3 that pole 1 is that pole with the greatest Doppler velocity shift begins to become apparent. The reasoning behind such a definition is due to the characteristics of weather and clutter modes. Because clutter modes are typically near Doppler zero and weather modes can be shifted some amount away from Doppler zero, the assumption can be made that if one of the

spectral modes is indeed a weather mode, then this mode will have a greater Doppler shift than the clutter mode present. Therefore, by classifying pole 1 and pole 2 in this manner, pole 2 will always have the classification of a clutter pole while pole 1 may or may not be classified as a weather pole.

Classification begins with the selection of features, or measurements used to distinguish between classes [21]. In this discussion, features will be limited to measurements of pole values independent of range cell number. Further research may incorporate pole values across a series of adjacent range cells for additional information which may enhance the ability of the classifier to distinguish between weather poles and non-weather poles. Taking this approach one step further, classification could draw upon previous classifications, which adds a time variable to the classification scheme. By increasing the scope of the classification process beyond a range cell-by-range cell decision, the negative effects of pole spreading and discrete clutter may be better eliminated. This extension to the pole classifier will be left as the topic of further investigation.

The classification scheme presented in this discussion consists of a two-dimensional feature space. The features chosen should be such that differences between the two decision classes are apparent, thus allowing for a decision to be made. One possible choice of features is the real component of each pole and the imaginary component of each pole. For a two-dimensional case such as the current estimation problem, plotting the two features against one another will usually give an indication as to the ability to form a reliable decision. Therefore, for the current problem, the feature space is the complex plane on which the values of pole 1 and pole 2 are to be plotted. Figures 4.6 and 4.7 are the values of pole 1 for both the simulated microburst event and the simulated clutter only event, while Figures 4.8 and 4.9 are the values of pole 2 for the same situations.

By comparing the values of pole 1 in Figures 4.6 and 4.7, any pattern differences between the two pole distributions may be attributed to the presence of a weather

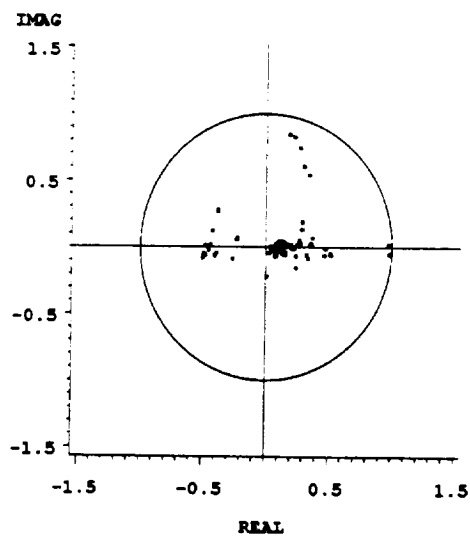


Figure 4.6 Complex Values of Pole 1 for Simulated Microburst and Clutter Return

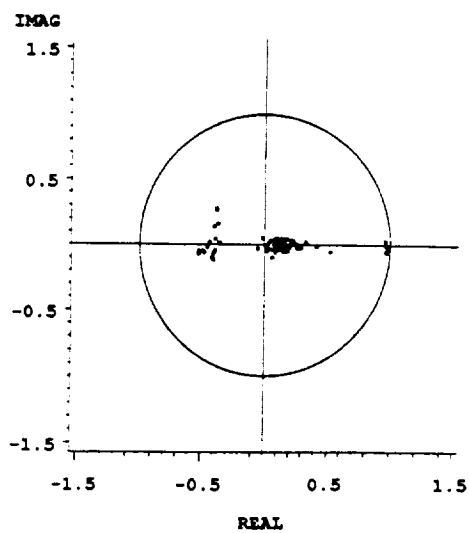


Figure 4.7 Complex Values of Pole 1 for Simulated Clutter Only Return

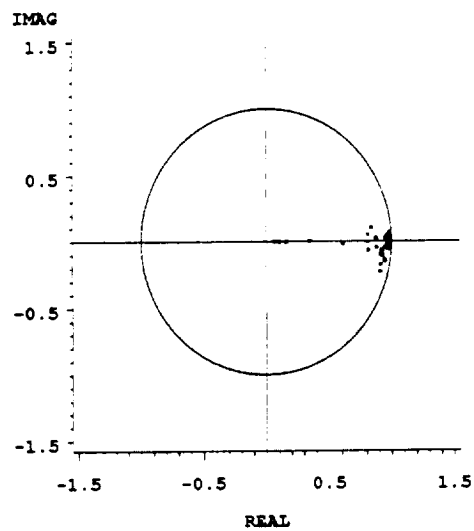


Figure 4.8 Complex Values of Pole 2 for Simulated Microburst and Clutter Return

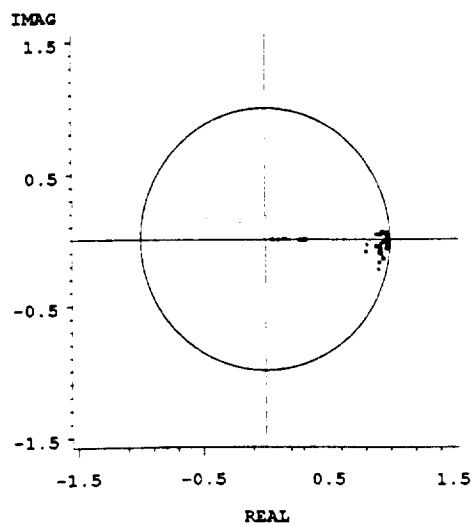


Figure 4.9 Complex Values of Pole 2 for Simulated Clutter Only Return

return in Figure 4.6. Although a difference does exist in that the weather and clutter simulation produced poles with larger positive imaginary components than the clutter only simulation, an improved choice of features may exist. Since windspeed estimation, or the Doppler velocity shift caused by a weather mode is the final objective, choose a polar representation for the set of features that includes (1) Doppler velocity and (2) complex pole magnitude. By plotting pole values in this revised feature space the weather pole and the clutter pole attributes become more apparent allowing for the feature space to be partitioned into decision regions where classifications can be made. Figures 4.10 and 4.11 are distributions of pole 1 in the polar feature space and Figures 4.12 and 4.13 are distributions of pole 2 in the same feature space.

Once a feature space is determined, the next step in classifying poles as weather or non-weather is to partition the feature space into decision regions where classifications can be made according to each pole's location in the feature space. In comparing Figure 4.10 with Figure 4.11, a group of poles is present in the microburst simulation that is not present in the clutter only simulation. The poles are between -10 m/s and -15 m/s Doppler velocity with magnitudes greater than 0.6. Upon comparing the scatter plots in feature space with the bubble plots, it can be determined that the group of poles mentioned are the same poles which reflect the leading edge of the microburst event recorded in range cells 20–28. As seen in Figures 4.12 and 4.13, the Doppler velocities associated with pole 2 are in the region near Doppler zero. For this reason pole 2 is always given the classification of clutter.

The decision regions which separate those poles classified as weather from those poles classified as non-weather will be determined through an analysis of pole distributions from a large collection of return data. The data used includes 10 simulated returns of the July 11th microburst event in Denver as well as 10 returns of the same situations without weather present. Although the decision regions determined from this data will be particular to the Denver area and the type of microburst included in the simulation, the approach to be discussed can be extended to any location or

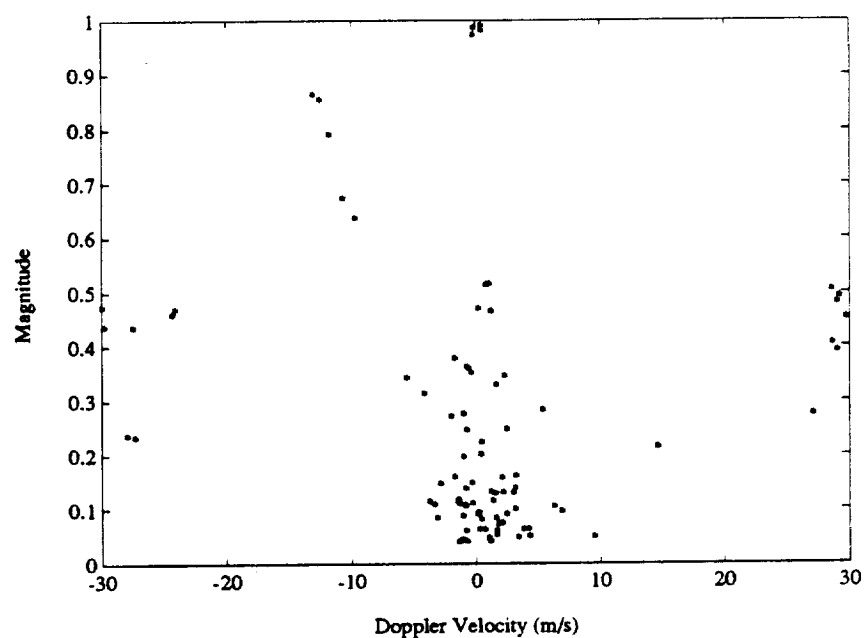


Figure 4.10 Polar Values of Pole 1 for Simulated Microburst and Clutter Return

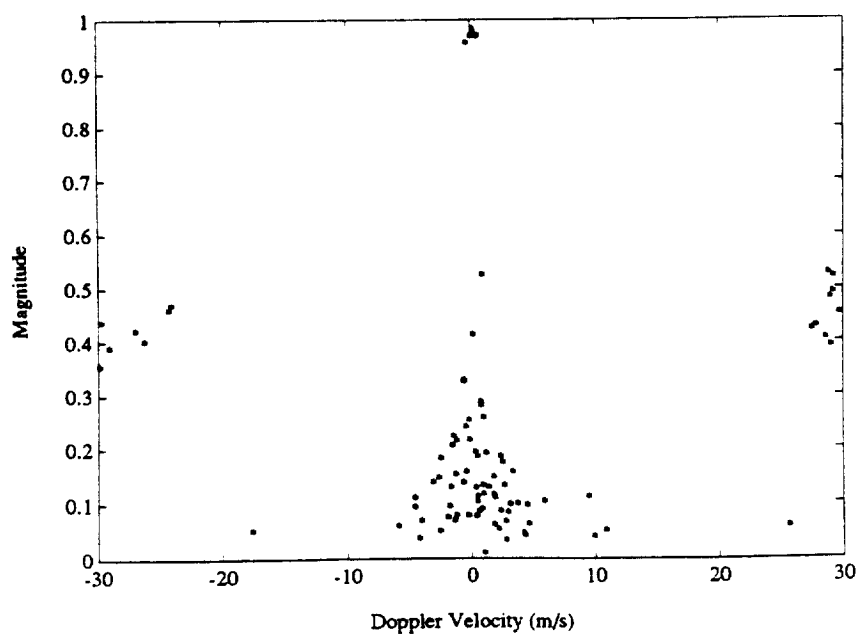


Figure 4.11 Polar Values of Pole 1 for Simulated Clutter Only Return

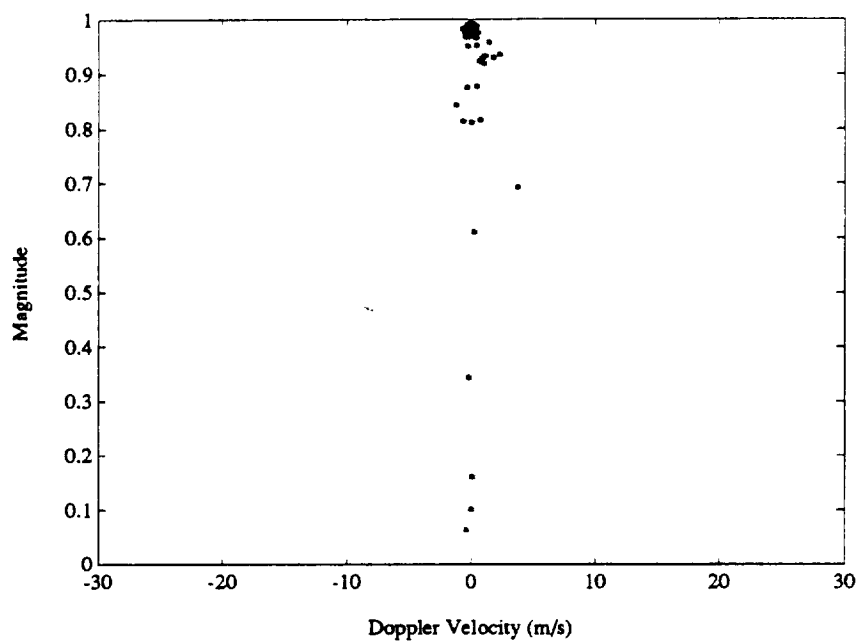


Figure 4.12 Polar Values of Pole 2 for Simulated Microburst and Clutter Return

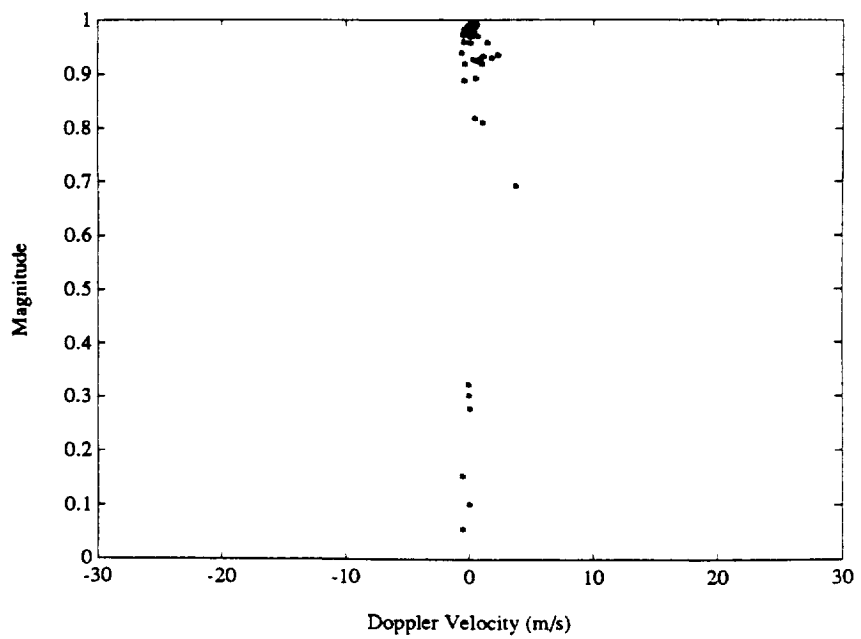


Figure 4.13 Polar Values of Pole 2 for Simulated Clutter Only Return

weather condition. A more complete analysis may include data which is distributed among a variety of locations and weather conditions and may reveal the optimum decision regions given all situations.

If weather poles and non-weather poles could always be separated due to their appropriate values then the classification scheme would be trivial. Unfortunately, weather poles and non-weather poles may occupy the same region in feature space. The decision boundary should be designed so as to minimize classification errors. Presented in Figures 4.14 and 4.15 are scatter plots of the pole locations for the simulated weather plus clutter and clutter only returns for 10 simulated runs. Note the existence of weather poles in Figure 4.14 which are not present in the clutter only simulations. The decision boundary has been empirically determined based on analysis of the pole locations and the apparent clustering of weather poles and non-weather poles. As the quantity and the types of data returns increases, a thorough analytical derivation of decision boundaries may be undertaken. The boundary in Figures 4.14 and 4.15 is a second order polynomial of the form

$$g(v) = \frac{v^2}{1.2v^2 + 450} + \frac{8}{v^2 + 12} \quad (4.1)$$

where v is Doppler velocity and $g(v)$ is the corresponding pole magnitude. The windspeed estimate for each range cell can thus be modeled by

$$\hat{v} = \begin{cases} v_1 & \text{for } g(v_1) < |\mu_1|^2 \\ 0 & \text{else} \end{cases} \quad (4.2)$$

Figure 4.16 details the complete algorithm which derives a windspeed estimate from an IQ data series using the two class pattern recognition classification procedure presented in this chapter.

By overlaying the windspeed estimate derived from a second order modal classifier along with a filtered pulse-pair windspeed estimate onto a bubble plot of the pole values, several characteristics of the classifier can be seen. In Figures 4.17 and 4.18

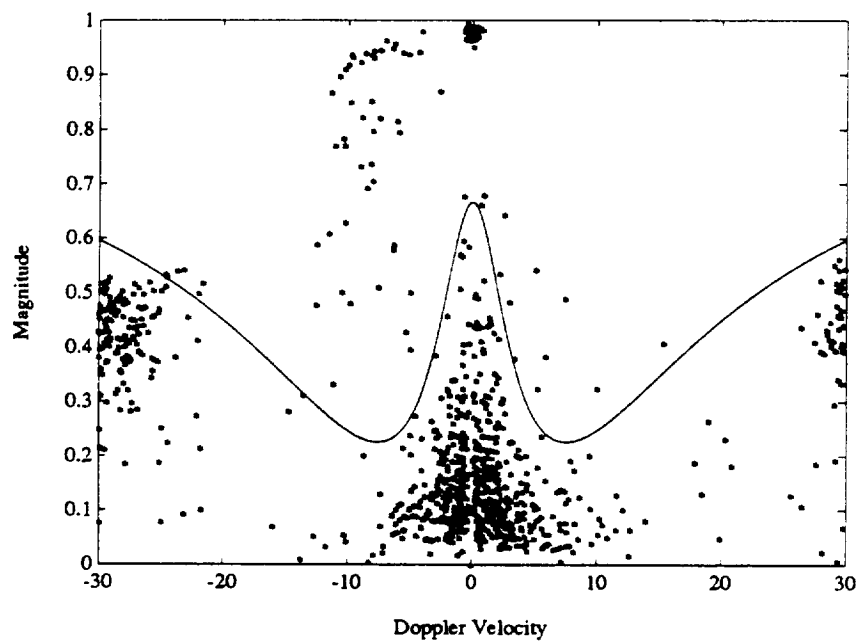


Figure 4.14 Polar Values of Pole 1 for 10 Simulated Microburst and Clutter Returns

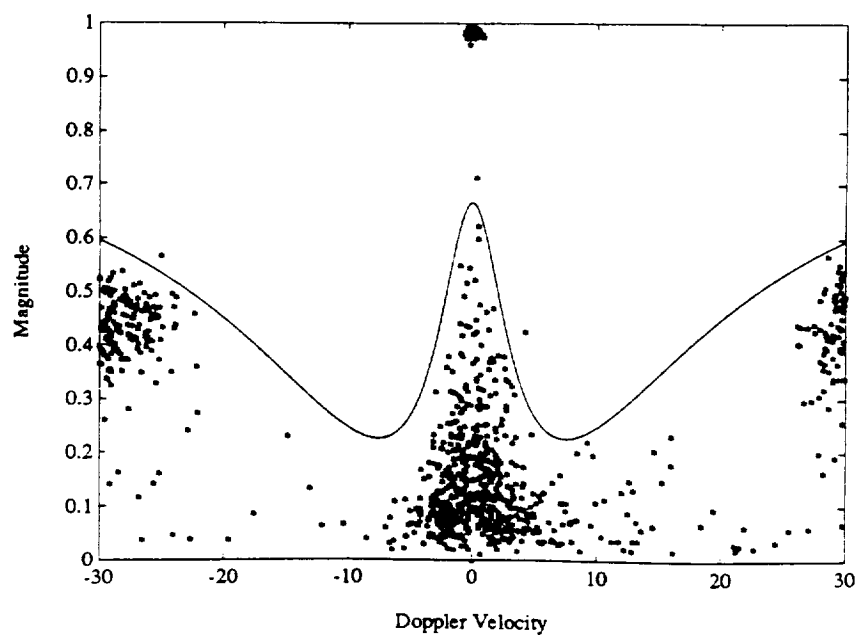


Figure 4.15 Polar Values of Pole 1 for 10 Simulated Clutter Only Returns

$$\begin{aligned}
\hat{R}(0) &= \frac{1}{N} \sum_{n=0}^{N-1} |x(n)|^2 \\
\hat{R}(1) &= \frac{1}{N} \sum_{n=0}^{N-2} x(n+1)x(n)^* \\
\hat{R}(2) &= \frac{1}{N} \sum_{n=0}^{N-3} x(n+2)x(n)^* \\
a_{11} &= -\frac{\hat{R}(1)}{\hat{R}(0)} \\
\sigma_1^2 &= (1 - |a_{11}|^2) \hat{R}(0) \\
a_{22} &= -\frac{1}{\sigma_1^2} [\hat{R}(2) + a_{11} \hat{R}(1)] \\
a_{21} &= a_{11} + a_{22} a_{11}^* \\
\mu_+ &= \frac{-a_{21} + \sqrt{a_{21}^2 - 4a_{22}}}{2} \\
\mu_- &= \frac{-a_{21} - \sqrt{a_{21}^2 - 4a_{22}}}{2} \\
v_+ &= \frac{-\lambda_o}{4\pi T_s} \arg(\mu_+) \\
v_- &= \frac{-\lambda_o}{4\pi T_s} \arg(\mu_-) \\
\mu_1 &= \begin{cases} \mu_+, & |v_+| \geq |v_-| \\ \mu_-, & \text{else} \end{cases} \\
\mu_2 &= \begin{cases} \mu_+, & |v_-| \geq |v_+| \\ \mu_-, & \text{else} \end{cases} \\
v_1 &= \frac{-\lambda_o}{4\pi T_s} \arg(\mu_1) \\
v_2 &= \frac{-\lambda_o}{4\pi T_s} \arg(\mu_2) \\
\hat{v} &= \begin{cases} v_1, & g(v_1) < |\mu_1| \\ 0, & \text{else} \end{cases}
\end{aligned}$$

Figure 4.16 Two Class Pattern Recognition Windspeed Estimator

observe that the windspeed estimate either passes through the pole with the greatest Doppler velocity, or it is set to zero. The pulse-pair estimator has a bias toward Doppler zero causing its windspeed estimates to be smaller than the modal estimates. Also notice that the poles with large Doppler shifts created through pole spreading have been removed by the classifier due to their small magnitudes. The pulse-pair windspeed estimates also contain some amount of editing from the pulse-pair spectral width estimator. When the spectral width becomes larger than a certain threshold value, such as 8 m/s in this case, the pulse-pair windspeed estimator is set to zero because the spectrum lacks a dominant spectral mode which causes the pulse-pair estimator to become erratic.

4.4 Second Coefficient Windspeed Estimator

By making the assumption that clutter modes will be primarily near Doppler zero, a simplification to the modal windspeed procedure can be achieved. Begin with the second order characteristic polynomial from (3.15) and solve for the coefficients a_1 and a_2 in terms of pole values

$$a_1 = -(\mu_1 + \mu_2) \quad (4.3)$$

$$a_2 = \mu_1 \cdot \mu_2 \quad (4.4)$$

Express (4.4) in polar form

$$a_2 = |\mu_1||\mu_2| \{ \cos(\theta_1 + \theta_2) + j \sin(\theta_1 + \theta_2) \} \quad (4.5)$$

where

$$\theta_1 = \arg(\mu_1) \quad (4.6)$$

$$\theta_2 = \arg(\mu_2) \quad (4.7)$$

By assuming that one pole will remain near Doppler zero, θ_2 , which is defined to have the smaller Doppler shift, will be nearly zero. With this assumption the

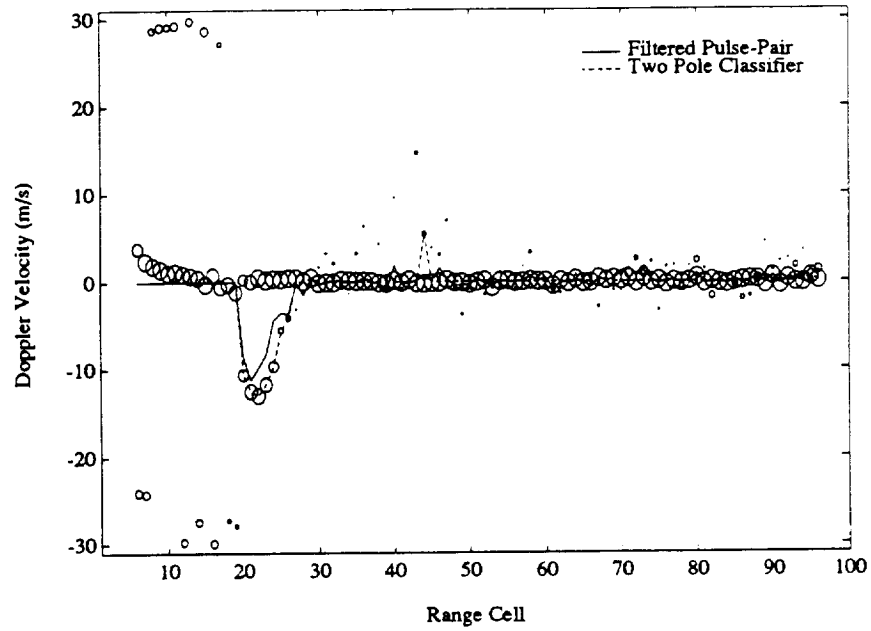


Figure 4.17 Bubble Plot with Windspeed Estimates for Microburst and Clutter

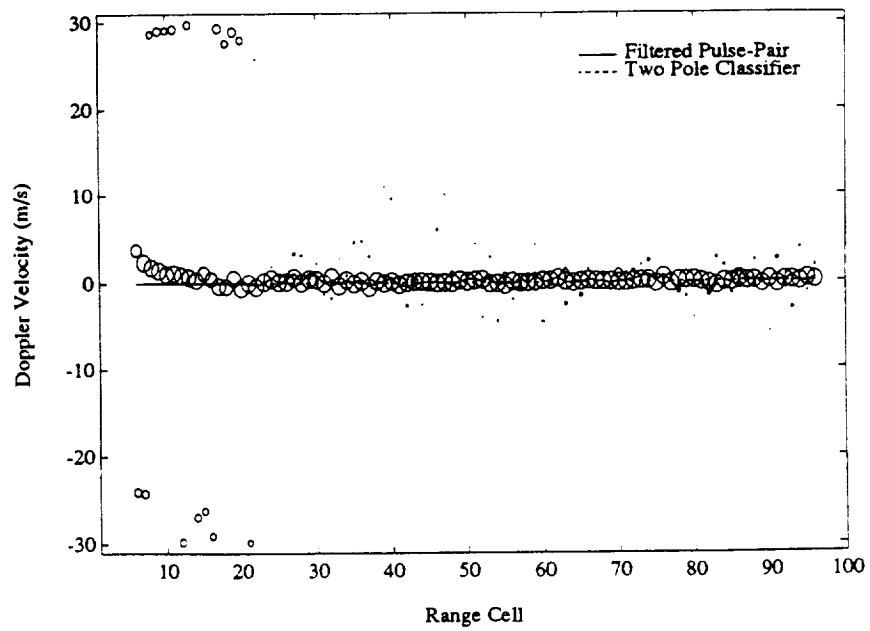


Figure 4.18 Bubble Plot with Windspeed Estimates for Clutter Only

argument of a_2 which is the sum of the arguments of both poles will be nearly equal to the argument of pole 1 (μ_1). The implication of this is that a savings of computational resources may be achieved with this approximation as shown in Figure 4.19. For this method the decision boundary can be applied directly to the polar value of the second AR coefficient a_2 without the need for computing poles or selecting pole 1 and pole 2 based on Doppler velocities.

5.1 Comparison of Windspeed Estimates

Begin the analysis by comparing windspeed estimates between techniques. In order to include all 42 frames of data, a three dimensional view of windspeed estimates is used. The pulse-pair estimates of windspeed provided the pulse-pair spectral width is less than 8 m/s are provided in Figures 5.1 and 5.2. The estimates have been set to zero for width values greater than the threshold. Figure 5.1 is a view of actual values for each range cell for each frame while in Figure 5.2 the estimates have been smoothed by averaging over a three cell by three frame region with the center cell and frame reflecting the average. In the smoothed plot windspeed trends are more readily seen which will aid in comparing estimation techniques. By observing these windspeed trends, characteristics of the microburst event can be seen. First, notice that the windspeed features are slanted in a diagonal direction from low frame and high range cell to a high frame number and a low range cell. This is created by the aircraft motion as it approaches and enters the microburst. At the first snapshot (frame 1) the event is seen in the larger range cells because the flight begins at a distance of about 8.5 km. During each successive frame the aircraft flies closer to the event which shifts its corresponding radar return in to closer range cells.

Another feature that can be seen in the windspeed plot is a valley that is located in front of a rising ridge. The valley is created by negative Doppler shifts which indicate a performance increasing headwind and the ridge indicates positive Doppler shifts which are induced by a performance decreasing tailwind. By putting these two features together while looking at the estimates from one frame only, the characteristic “S”-curve pattern appears. These windspeed “slices” for each frame are included in Appendix B.

For a two pole classifier which will be applied to the Orlando event 143, begin by observing the distribution of pole 1 for all frames, given in Figure 5.3. Notice that the boundary $g(v)$ which was determined for the simulated situation in Chapter 4 has been overlaid onto the pole distribution for this situation as well. The feature

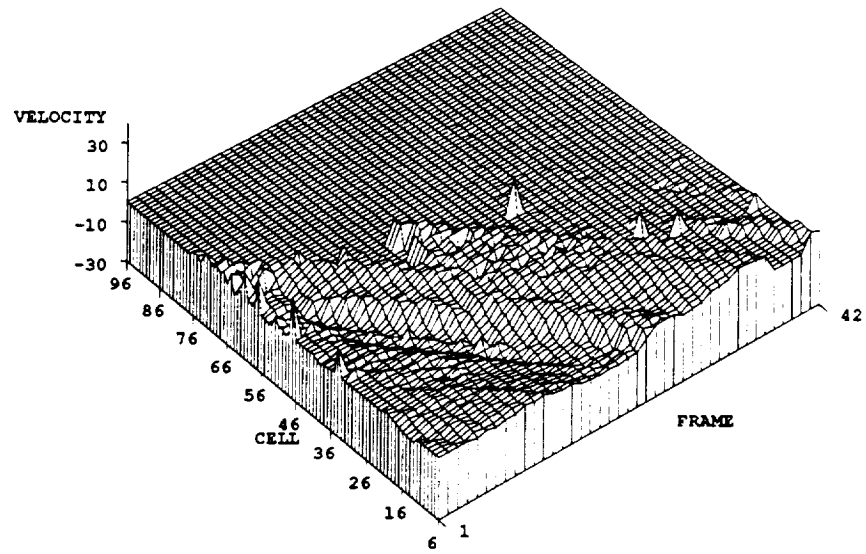


Figure 5.1 Pulse-Pair Velocity Estimates for Event 143

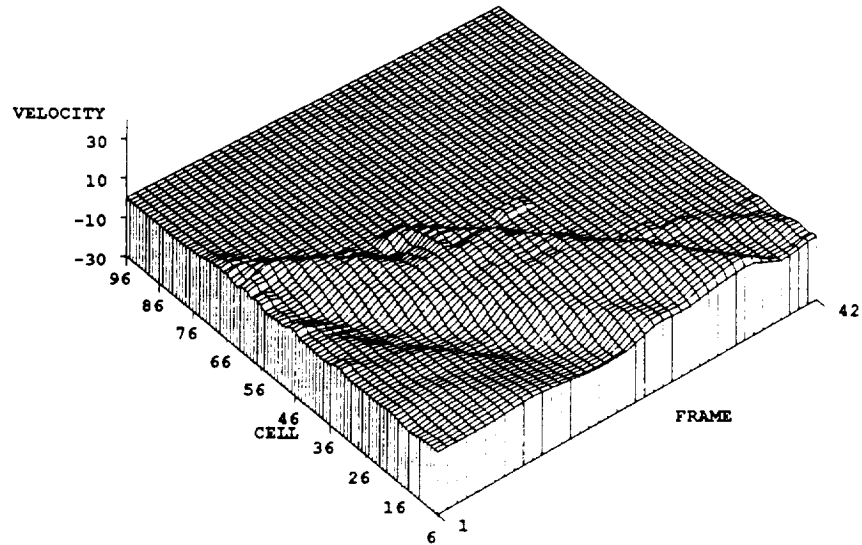


Figure 5.2 Pulse-Pair Velocity Estimates for Event 143. smoothed

space boundary in this analysis will reflect simulated data on account of the lack of any clutter only data available at the present time for the Orlando area. A decision boundary determined from a situation which does not have both weather plus clutter and clutter only data will most likely not yield results that are as good as when both cases are available. For this reason, the classifiers presented in this chapter will use the decision boundary determined in Chapter 4.

As the volume of useful clutter data increases, analyses of pole value distributions at certain locations, antenna elevations, and azimuths, may indicate that one decision boundary for a particular location is not sufficient. It may be beneficial to implement several decision boundaries depending upon these or other factors. At the present time it is not known how pole distributions change, given these factors. This analysis will be left for future research as more data becomes accessible.

By implementing the two pole classifier as specified in Chapter 4 with the decision boundary as shown in Figure 5.3, the estimated values of windspeed are computed and shown in Figures 5.4 and 5.5. Again, Figure 5.5 contains a smoothed sample of the windspeed estimates. It is now possible to compare the two pole classifier with the pulse-pair estimator over several range cells. Notice that the general shape of both estimators is similar in that both contain the diagonal valley and ridge. To compare windspeed magnitudes refer to the individual frame plots included in Appendix B.

One feature that is present in the two pole classifier that is not present in the pulse-pair estimator is peaks of large Doppler velocities which occur primarily in the range cells following the microburst event. These peaks result from range cells where pole spreading occurs and the classifier assigns the spread pole as weather instead of recognizing it as clutter. This error can be seen in the pole scatter plot (Figure 5.3) as those poles with a large Doppler velocity and are large in magnitude. These poles do not appear to fit with the cluster of weather poles, seen as large magnitude poles with Doppler velocities between ± 10 m/s. The classifier can not differentiate between these poles and weather poles due to them being located in a region where weather poles

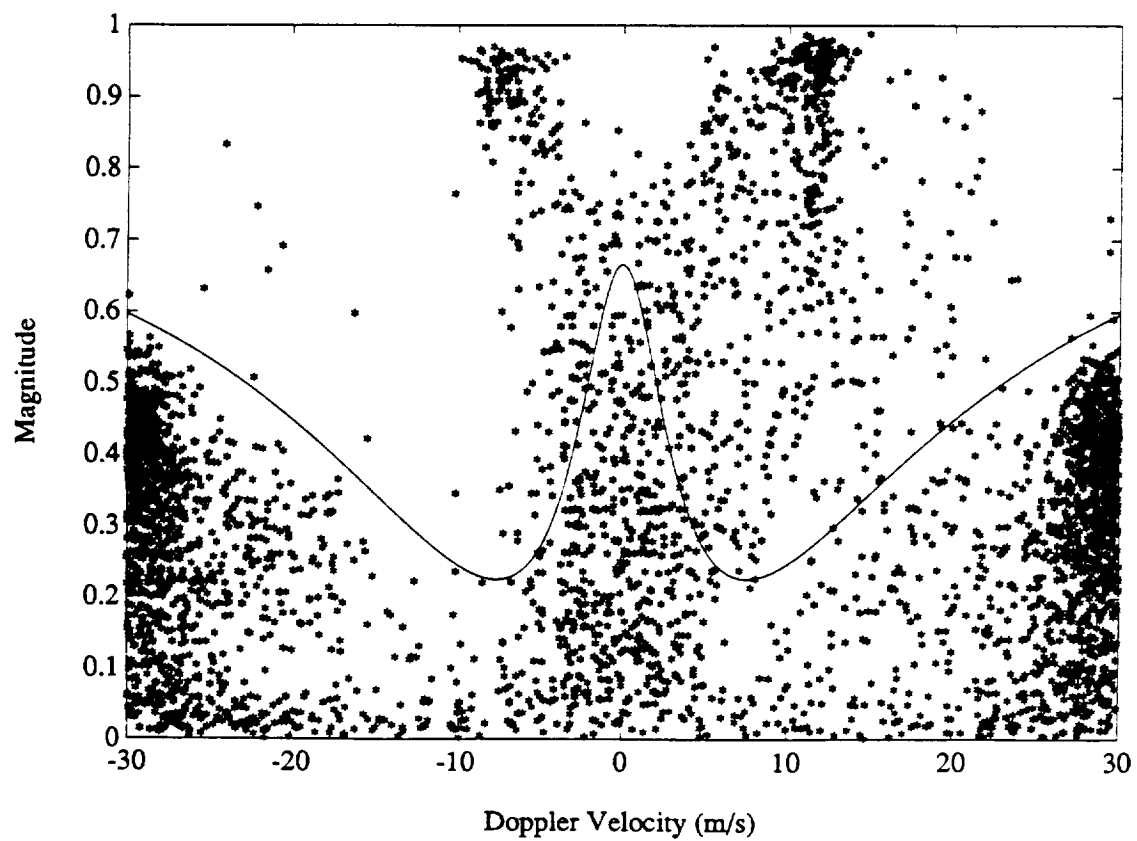


Figure 5.3 Pole 1 Values for Event 143

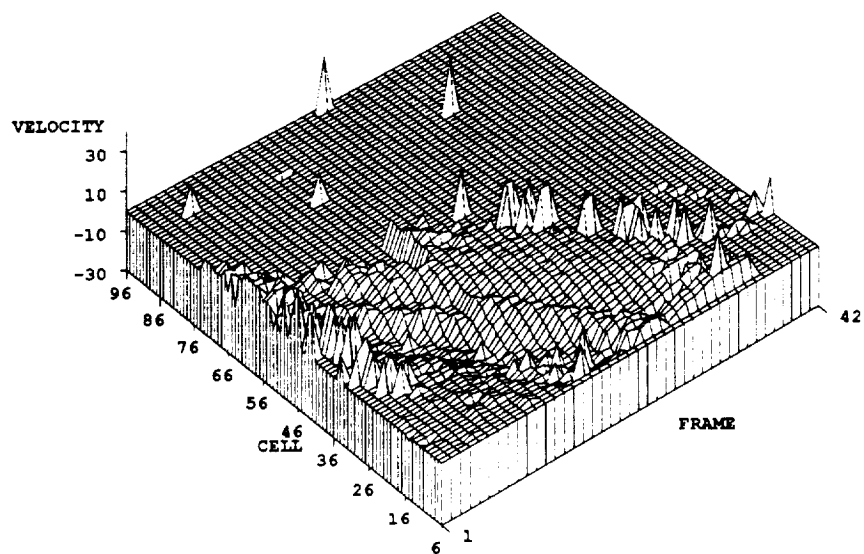


Figure 5.4 Two Pole Classification Estimates for Event 143

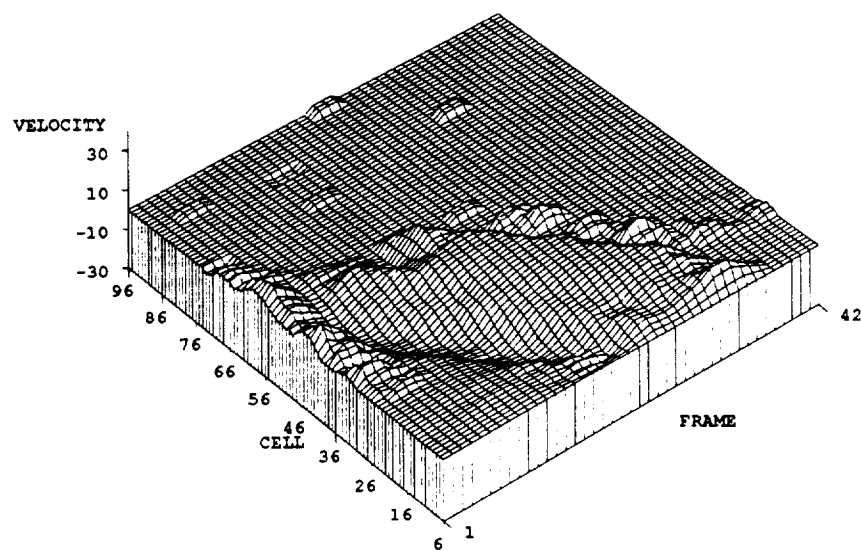


Figure 5.5 Two Pole Classification Estimates for Event 143. smoothed

may appear. Rejecting these poles by altering the decision boundary will enhance estimation for this particular case, but may remove important weather poles when used in another situation.

The next windspeed estimator that will be examined is the second coefficient estimator. As shown in Chapter 4 this is a simplified version of a two pole classifier which assumes at least one pole will be near Doppler zero for a reliable windspeed estimate. In this method the decision boundary is applied to the second AR coefficient rather than the pole with the greatest Doppler velocity. Since the second AR coefficient is the product of the two complex poles, the difference between the second coefficient and pole 1 is the value of pole 2. For returns with mostly stationary clutter the value of pole 2 will be approximately 1. Figure 5.6 is a scatter plot of second coefficient values which closely matches the scatter plot formed from pole 1 values (Figure 5.3). By applying the same decision boundary to the second coefficient that was applied to pole 1 in the two pole classifier, the windspeed estimates given in Figures 5.7 and 5.8 are produced.

A comparison between the unsmoothed windspeed estimates from the second coefficient and the two pole classifier reveals that the two estimators yield similar results for this situation. Some differences that can be noted are the apparent reduction of misclassifications in the second coefficient estimator which results in fewer isolated peaks in the velocity estimate plots. This may be attributed to the second coefficient having a smaller magnitude than pole 1 as a result of its multiplication by pole 2 which has a magnitude less than unity. Having a slightly smaller magnitude will tend to increase the probability that the second coefficient will be below the decision boundary threshold and will be set to zero when pole 1 may be above the threshold. It can be observed in the single frame plots included in Appendix B that the second coefficient estimator is more often set to zero than the two pole classifier. This relation may indicate that separate decision boundaries may be required for each type of windspeed estimator.

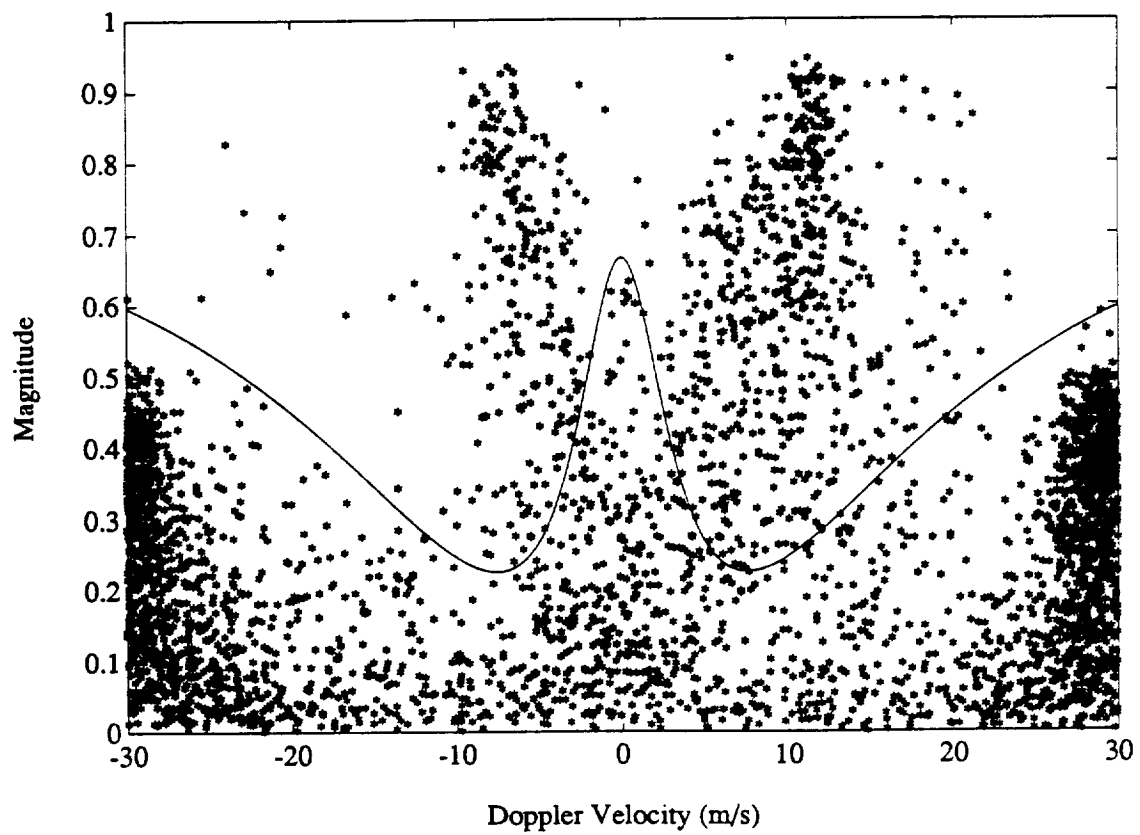


Figure 5.6 Values of Second AR Coefficient for Event 143

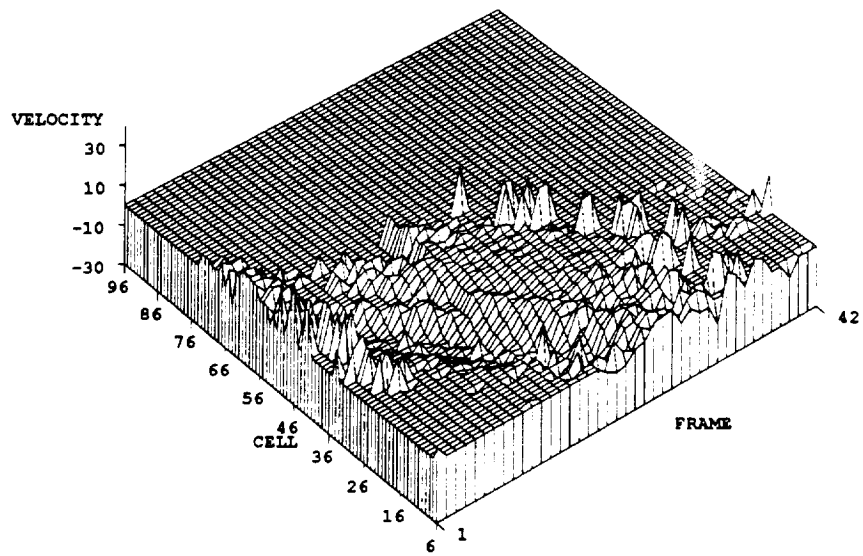


Figure 5.7 Second Coefficient Velocity Estimates for Event 143

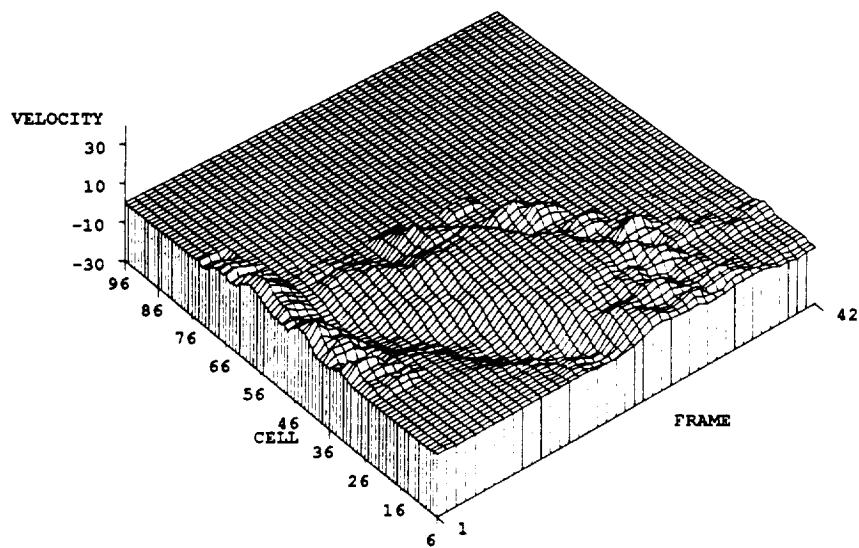


Figure 5.8 Second Coefficient Velocity Estimates for Event 143, smoothed

By further comparing the windspeed estimates provided in Appendix B, several more observations can be made about the filtered pulse-pair, the two pole classifier, and the second coefficient estimator. First, notice that the two modal analysis methods generate similar results which indicates that a windspeed estimate computed directly from AR coefficients may be feasible. Compared to the pulse-pair method, modal analysis tends to generate larger windspeed estimates, which can be attributed to the clutter bias present in the filtered pulse-pair estimates. On the other hand, the modal analysis results appear to be more erratic than the pulse-pair estimates. This is seen more in both the first group of range cells and the last group of range cells where the microburst return is not as strong. The erratic behavior of the modal estimates may be improved by implementing a more accurate decision boundary and forming windspeed estimates from pole values beyond the current range cell.

5.2 Comparison of Hazard Factors

The hazard factor values computed in this discussion are derived from the weighted least-squares procedure discussed in Chapter 2. The hazard factor is computed for each frame and the results are recombined to produce another three dimensional plot similar to the windspeed estimate plots presented earlier. Figures 5.9 – 5.14 are included and contain hazard factor values for the windspeed estimators being compared. For clarity, only hazard factor values which exceed a threshold of 0.1 are included. The remaining values are set to zero in the plot. In this way, the regions with a possible hazard are emphasized. Also presented with the three dimensional surface plot of hazard factor is a contour plot of the same data. The contour plot assists in locating exactly which frames and corresponding range cells contain a hazard factor above the threshold.

In comparing between the hazard factor values for all three windspeed estimators, all reflect a diagonal line where the hazard factor exceeds the threshold. This line corresponds to the diagonal valley and ridge seen in all windspeed estimates. The

hazard line is a result of a detected headwind (the valley) which is followed by a tailwind (the ridge). The hazard factor is an attempt to measure the amount of performance loss which an aircraft could expect to encounter by proceeding through the forward-looking region.

Upon closer examination of the hazard factor values, some differences between the three techniques become apparent. One of the more obvious differences may be the existence of two parallel hazard lines in the modal analysis techniques while the pulse-pair shows only one diagonal hazard factor line. This can be attributed to the modal classifier assigning zero windspeed estimates to weather poles in a region near Doppler zero. This creates a flat segment in the windspeed estimates where the "S"-curve crosses zero velocity. The hazard factor is reduced when it encounters this flat segment, but is large on either side where the windspeed estimates diverge. Also, the pulse-pair estimator includes fewer spurious peaks in the hazard factor, while the two pole classifier includes the most spurious hazard peaks. When comparing magnitudes of the hazard factors, all contain values between 0.1 and 0.2 for the diagonal lines. A difference does exist, however, in the magnitudes of the isolated hazard peaks. The pulse-pair estimator not only has fewer isolated peaks, but these peaks have magnitudes that are smaller than the peaks originating from the modal analysis methods.

5.3 Fixed Range Time Scan

In a typical pulse Doppler radar system the signal processing involved will work with the data in the form of energy returns from a number of incremental range cells, each a specified distance from the radar antenna. In this way, the processing of the data is nearly simultaneous over a spatial region. For radar systems that have a moving platform, such as an airborne system, a different technique may be employed that analyzes data by fixing the radar scan range to one spatial distance and processing additional data over time as the aircraft moves through the spatial

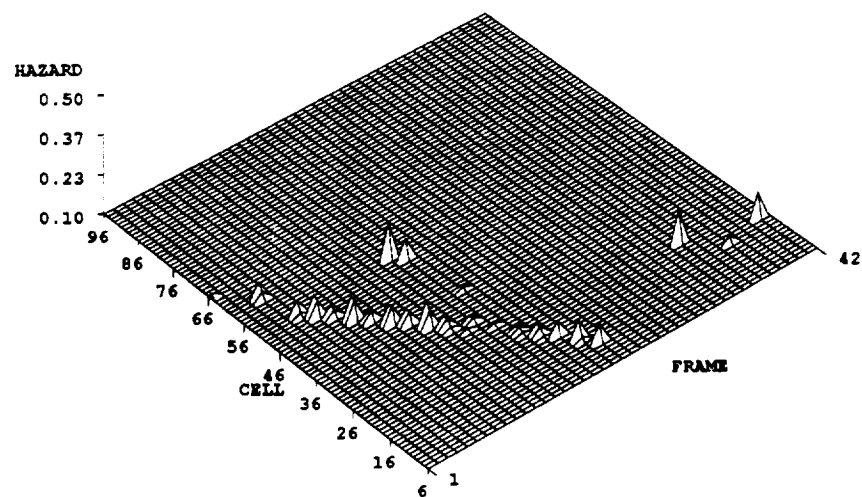


Figure 5.9 Pulse-Pair Hazard Factor for Event 143

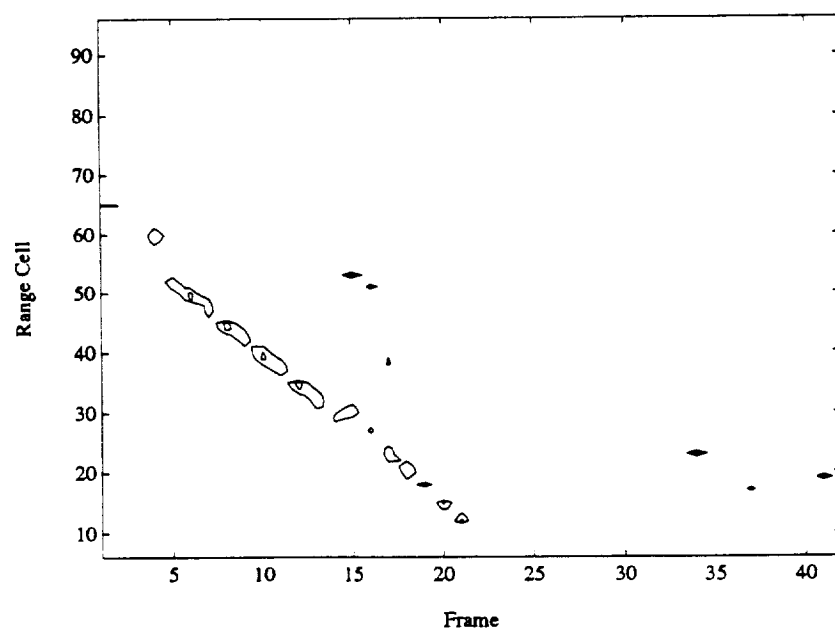


Figure 5.10 Contour of Pulse-Pair Hazard Factor for Event 143

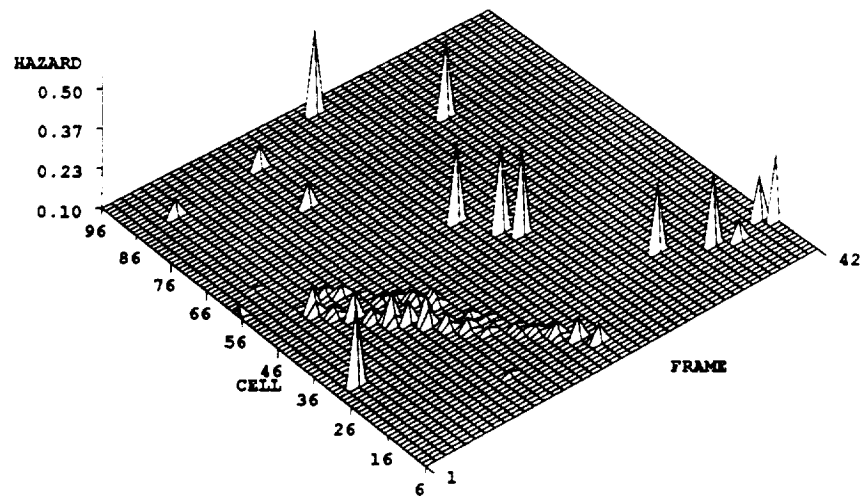


Figure 5.11 Two Pole Classifier Hazard Factor for Event 143

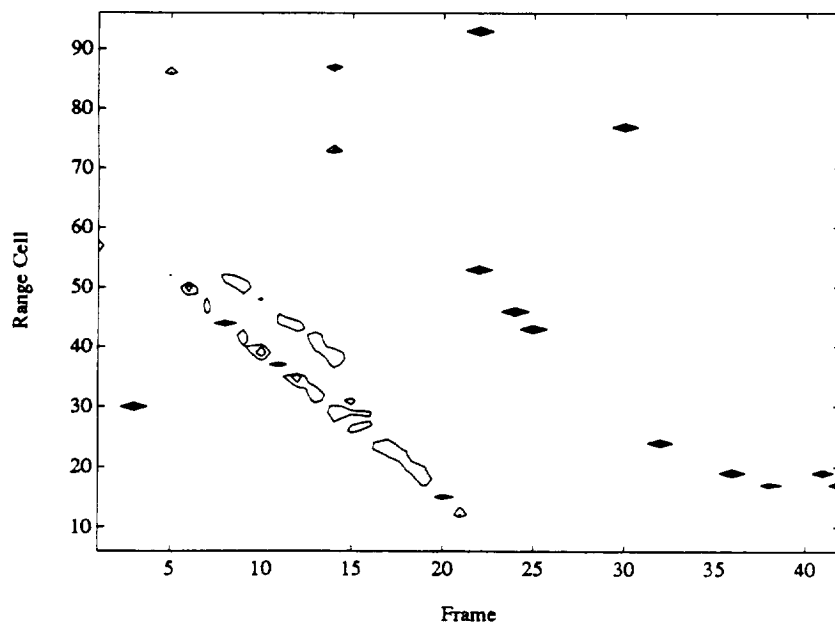


Figure 5.12 Contour of Two Pole Classifier Hazard Factor for Event 143

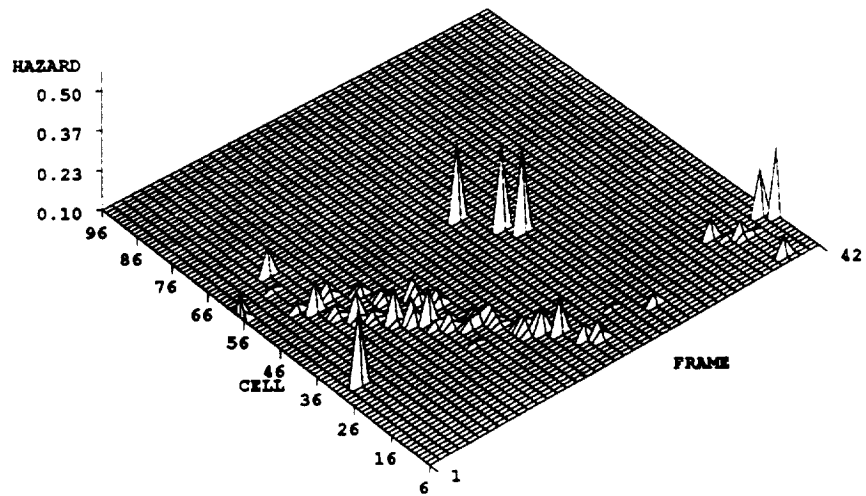


Figure 5.13 Second Coefficient Classifier Hazard Factor for Event 143

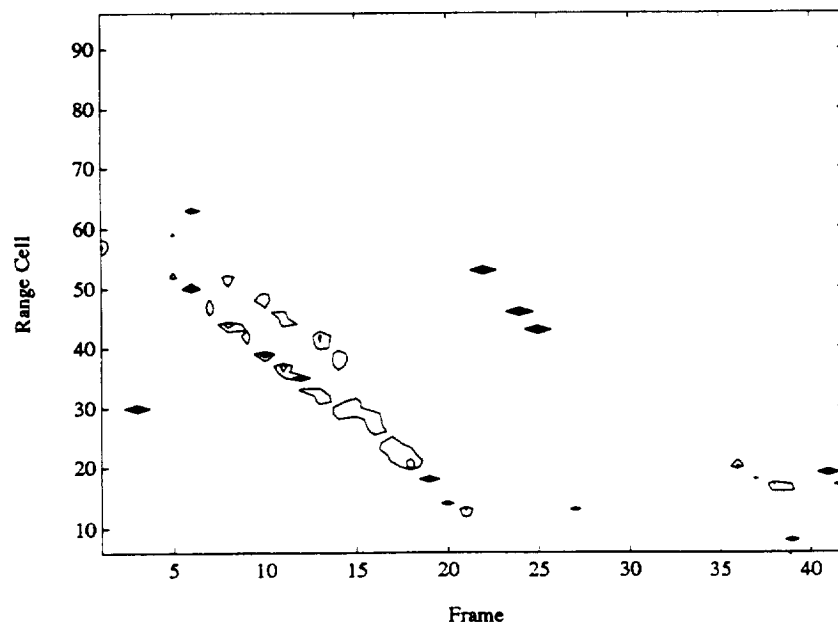


Figure 5.14 Contour of Second Coefficient Classifier Hazard Factor for Event 143

region. This type of processing will be referred to as a fixed range time scan. A depiction of both a snapshot return and a fixed range time scan return are given in Figures 5.15 and 5.16.

One method for understanding how a fixed range time scan functions in comparison to a snapshot is to look again at windspeed estimates for several range cells and several frames such as Figures 5.9, 5.11 and 5.13. Recall that a typical snapshot would process all range cells one frame at a time. This can be visualized by separating the three dimensional plot into a series of two dimensional plots that contain one frame number each. The slicing of the plot in this way is illustrated in Figure 5.17.

The fixed range time scan processes data from a fixed distance over time. This can be visualized by slicing the three dimensional plot into individual range cells with all frames included. Figure 5.18 is an illustration of this method. The frames become a time axis due to the sequential order in which they are recorded. For this situation, which is a two pole classification estimator of the Orlando event, each range cell represents approximately 2.8 seconds, which is the amount of time required for the antenna sweep pattern to cross zero azimuth. Because the valley and ridge features of the microburst are diagonal to both frame and range cell, it is possible to take slices from either a fixed range (cell) or a fixed time (frame).

One advantage of a fixed range time scan is that all returns will occur from the same range which balances the quality of the return across the spatial region. In a snapshot, returns from the farther range cells will suffer from signal attenuation while the closer range cells contain strong returns. The fixed range time scan allows the return data from a spatial region to be processed as soon as it enters a specified region of the aircraft. In this way, processing can be compared to an in situ windspeed estimator that is positioned at a fixed distance in front of the aircraft. The processing of data to derive a hazard factor would be similar to an in situ hazard processor. More than one fixed range could be specified in order to allow for different warning intervals based on the ability of the radar system to detect a hazard. Strong hazards could be

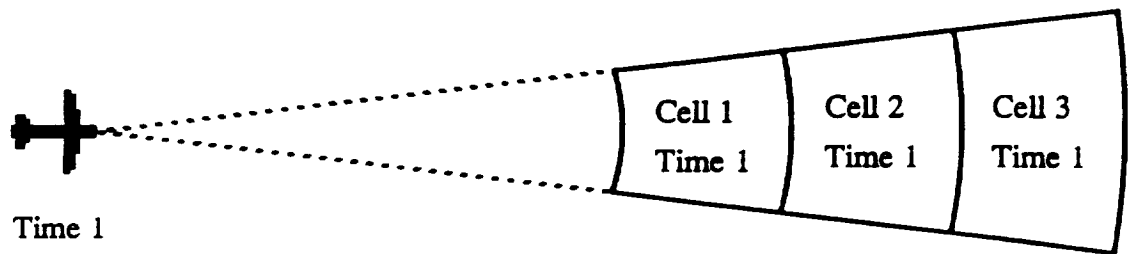


Figure 5.15 Snapshot

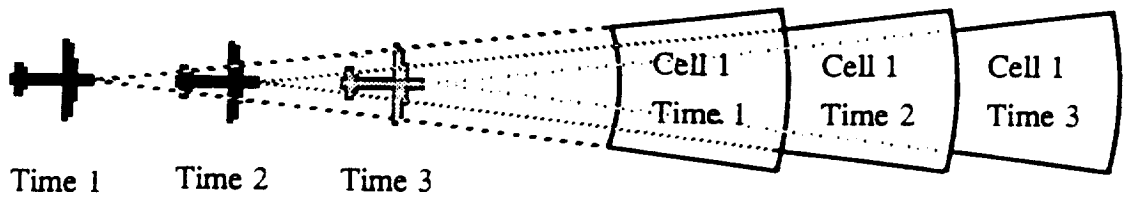


Figure 5.16 Fixed Range Time Scan

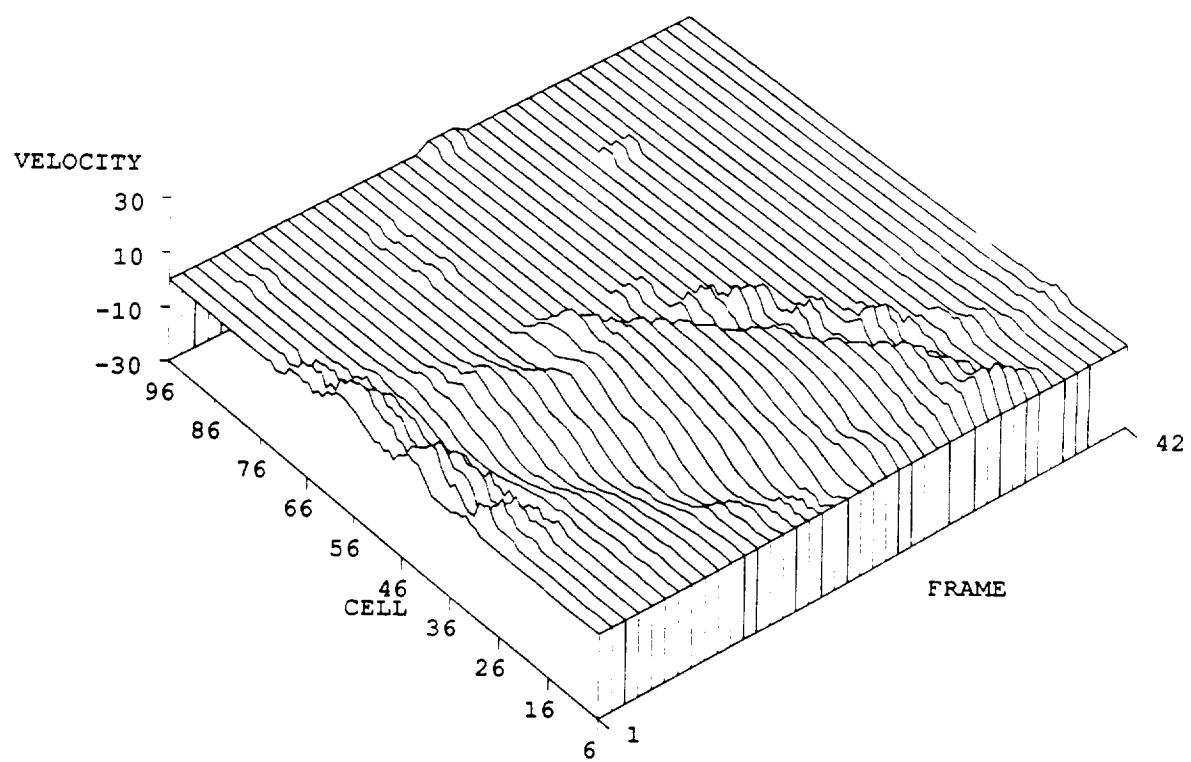


Figure 5.17 Illustration of Snapshot Processing

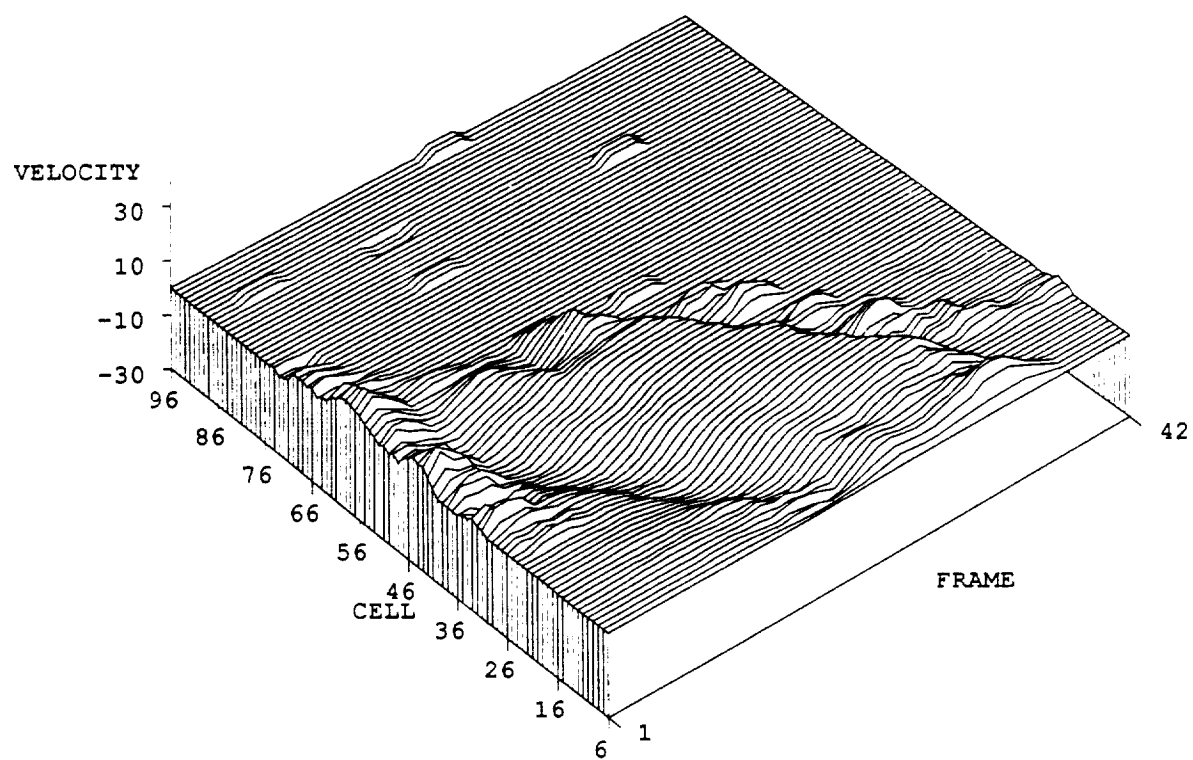


Figure 5.18 Illustration of Fixed Range Processing

detected with a greater warning time while events with weaker returns might require a closer range and thus, less warning time.

Finally, the fixed range time scan could work in conjunction with typical radar snapshots by providing an additional viewpoint to the current situation. By providing feedback to the information gained by radar snapshots, a fixed range time scan could increase the reliability of the estimates generated.

CHAPTER 6

CONCLUSIONS

With conventional signal processing techniques the ability of an airborne pulse Doppler radar system to successfully detect the presence of a hazardous windshear condition such as a microburst relies heavily upon the correct estimation of windfield characteristics. The presence of ground clutter for aircraft operating at low altitudes in and near urban terminal areas inhibits the radar's ability to clearly resolve wind-speed estimates. Typically the solution to this problem is to attempt to remove the effect of clutter with clutter rejection filters. With Doppler spectrum modal analysis as presented and discussed in this thesis, the clutter is not removed by filtering, but modeled along with any weather return and discarded through a mode classifier. If classified correctly, the weather mode has the potential to yield a windspeed estimate which lacks bias from the clutter mode due to the separate modeling of the clutter return.

Modal analysis of Doppler radar data applied to windspeed estimation possesses several favorable attributes over more conventional methods such as the pulse-pair estimator. Among these attributes are a low computational load due to the absence of clutter rejection filtering and the ability to yield unbiased windspeed estimates even in low signal-to-clutter environments. Unfavorable attributes of modal analysis include variance in the windspeed estimates resulting from misclassification of some poles, which increases the probability of false alarm. An improved pole classification scheme should be addressed in future research.

Currently, one disadvantage of modal analysis is the lack of an optimal method for determining the decision boundary in the pole classifier. This is primarily due to the limited amount of flight data available from which to form a statistical model of the poles. As flight data becomes more accessible, more complete knowledge of

clutter characteristics can be obtained, which should increase the effectiveness of pole classifiers. Classification beyond the scope of a single range cell should add stability to windspeed estimates as well as reduce the adverse effects of pole spreading and discrete clutter.

The classification nature of modal analysis lends itself to advanced areas such as pattern recognition and neural computing. Pattern recognition routines may be able to detect hazardous windshear conditions through direct processing of radar IQ data without the need for computing windspeed estimates. For example, a pattern recognition routine formulated as a data transformation algorithm might be trained to recognize the “S”-curve characteristic of a microburst. Then windshear signatures across time and/or azimuth can be combined and averaged to improve the ability to recognize and detect a hazardous condition.

It may also be possible to formulate a more robust windspeed estimator based on a combination of two or more individual estimators. Because each type of estimator has certain strengths and weaknesses, an integration of several estimators could lead to better results by using the best aspects of each system. For example, by using pulse-pair estimates in conjunction with a two pole model, the confidence in detecting hazards may be increased.

Finally, by examining data presented through a fixed range time scan, windfield estimates can be obtained in a method analogous to a predictive in situ hazard detector. Since each estimate is obtained as the aircraft is moving through a spatial region with a constant radar range, signal attenuation remains nearly constant. In comparison, a radar snapshot will contain close range cells with little attenuation and farther range cells with much attenuation.

APPENDICES

Appendix A

Autoregressive Modeling

Autoregressive (AR) modeling is a popular form of spectral estimation due to a relatively low computational power required and an improved spectral resolution over conventional FFT approaches [16]. AR models are an all-pole model having the following spectral density:

$$\mathcal{P}_{AR}(f) = \frac{\sigma^2 \Delta t}{\left| 1 + \sum_{k=1}^p a_k \exp(-j2\pi f k \Delta t) \right|^2} \quad (\text{A.1})$$

where Δt is the sampling interval of the process. An AR model of order p requires the estimation of the parameters $\{a_1, a_2, \dots, a_p, \sigma^2\}$, where p can be any positive integer. Presented here will be the Levinson–Durbin algorithm for fitting the AR parameters to a set of sample data. Other methods of AR modeling exist and are discussed by Kay and Marple [16] and Keel [9].

A.1 Levinson–Durbin Algorithm

This is an iterative procedure for computing the p th order AR parameters associated with a complex series x_n based on the relationship between the AR parameters and the autocorrelation function of the complex series. In matrix form the relationship is described by

$$\begin{bmatrix} R_{xx}(0) & R_{xx}(-1) & \cdots & R_{xx}(-p) \\ R_{xx}(1) & R_{xx}(0) & \cdots & R_{xx}(-(p-1)) \\ & & \ddots & \\ R_{xx}(p) & R_{xx}(p-1) & \cdots & R_{xx}(-0) \end{bmatrix} \begin{bmatrix} 1 \\ a_1 \\ \vdots \\ a_p \end{bmatrix} = \begin{bmatrix} \sigma^2 \\ 0 \\ \vdots \\ 0 \end{bmatrix} \quad (\text{A.2})$$

where the autocorrelation estimate of x_n is given by

$$R_{xx}(m) = \frac{1}{N} \sum_{n=0}^{N-m-1} x_{n+m} x_n^* . \quad (\text{A.3})$$

This relationship can assume several forms, but in general is known as the Yule-Walker equations [16]. The Levinson-Durbin algorithm iterates through successively higher order AR parameter sets $\{a_{11}, \omega_1^2\}, \{a_{21}, a_{22}, \omega_2^2\}, \dots, \{a_{p1}, a_{p2}, \dots, \omega_p^2\}$ where a_{ki} refers to the i th coefficient of the k th order AR model. The procedure stops when the desired model order is reached. Begin the algorithm with the first order model parameters

$$a_{11} = -\frac{R_{xx}(1)}{R_{xx}(0)} \quad (\text{A.4})$$

$$\sigma_1^2 = (1 - |a_{11}|^2)R_{xx}(0) . \quad (\text{A.5})$$

Higher order parameters are recursively computed as follows:

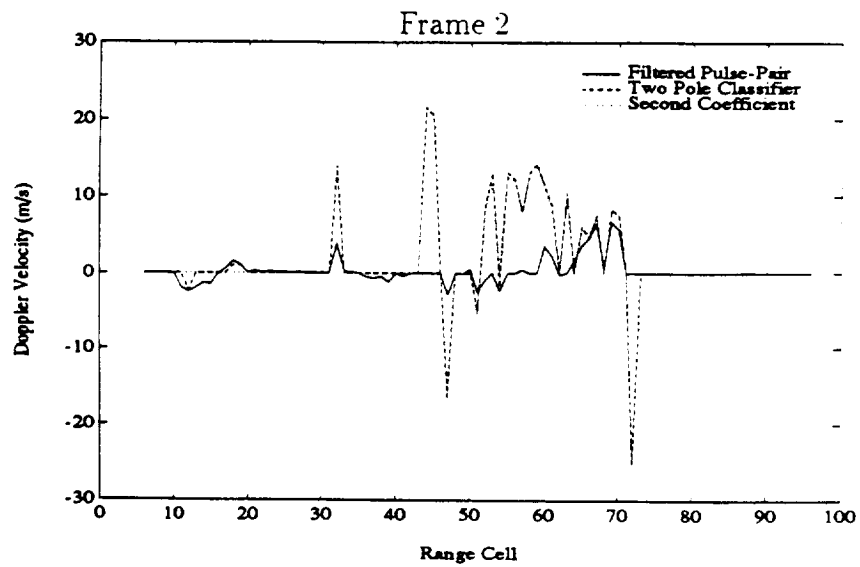
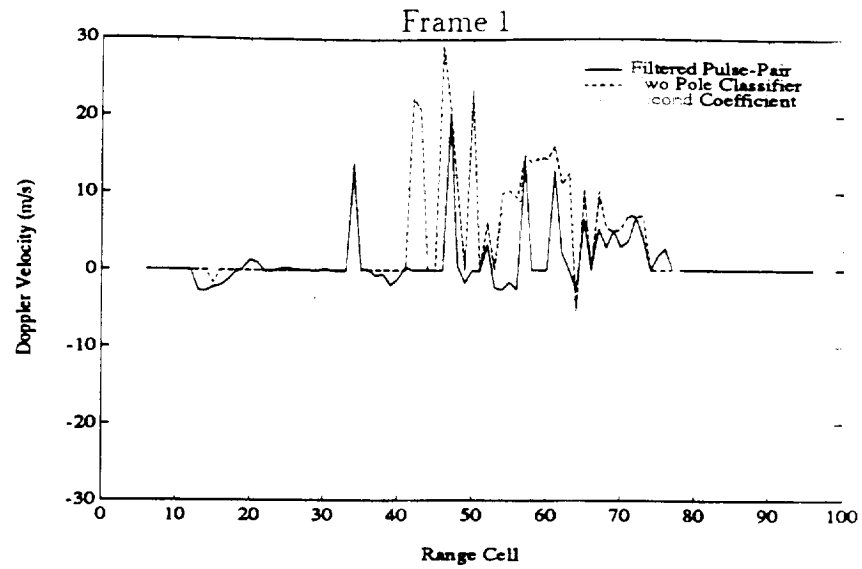
$$a_{kk} = -\frac{1}{\sigma_{k-1}^2} \left[R_{xx}(k) + \sum_{l=1}^{k-1} a_{k-1,l} R_{xx}(k-l) \right] \quad (\text{A.6})$$

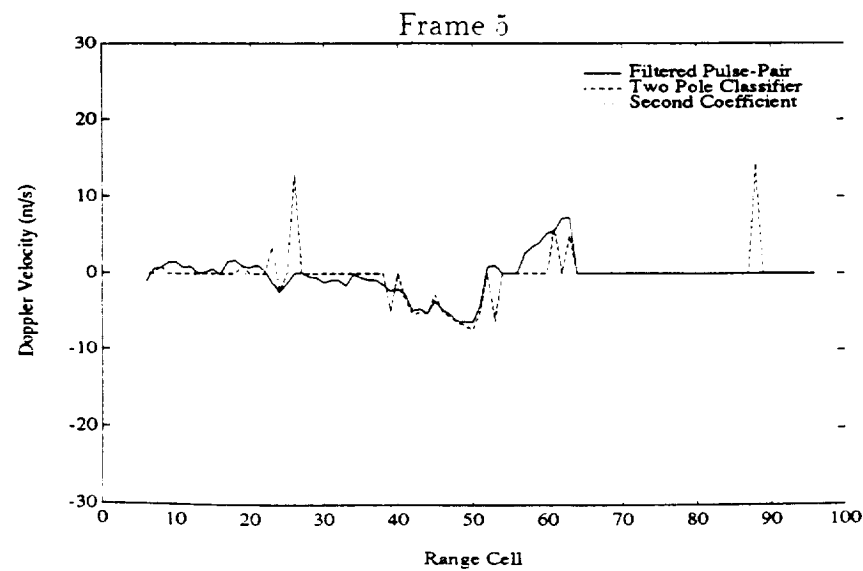
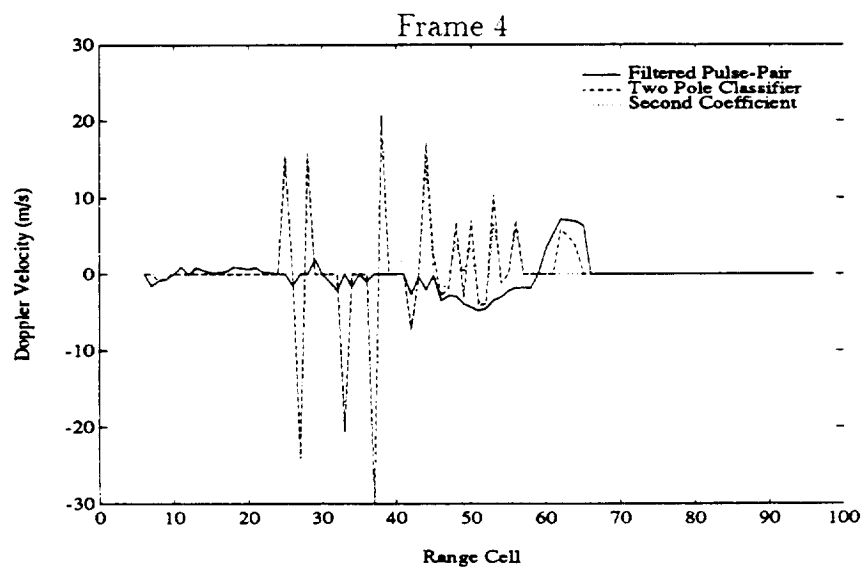
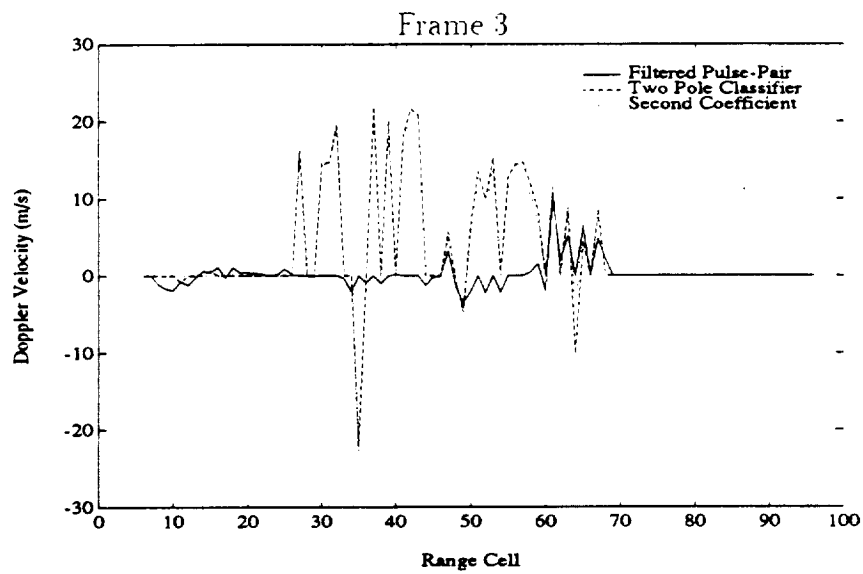
$$a_{ki} = a_{k-1,i} + a_{kk} a_{k-1,k-i}^* \quad (\text{A.7})$$

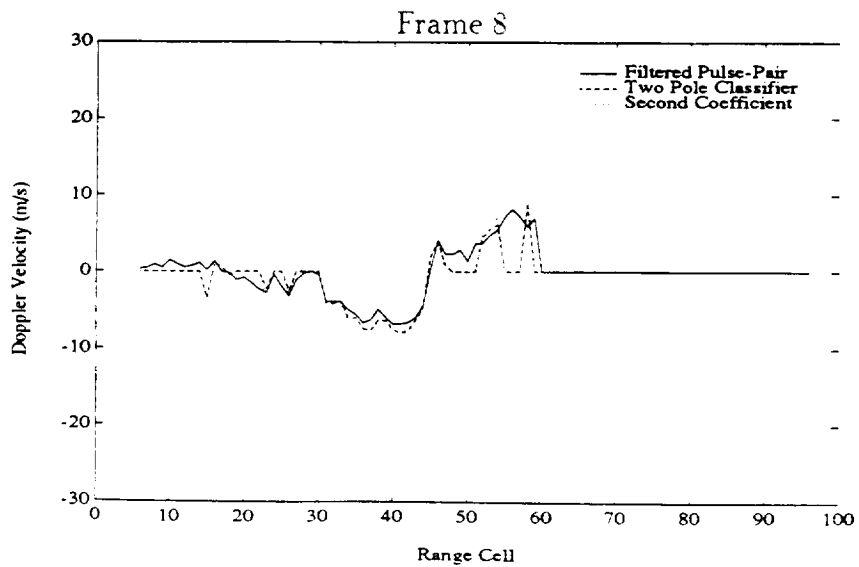
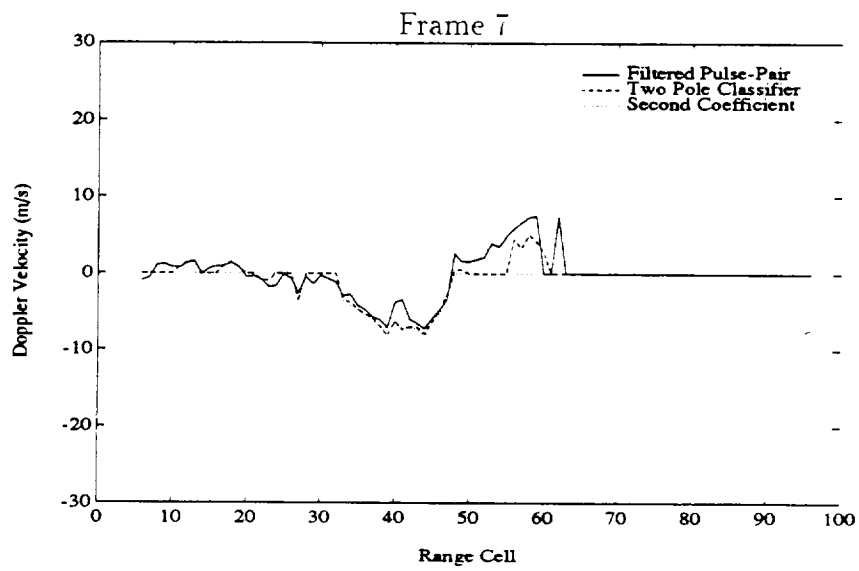
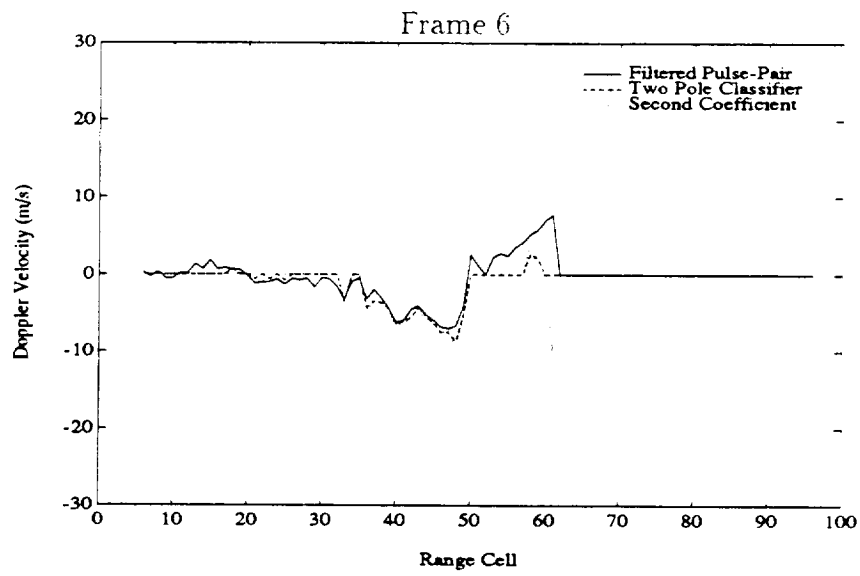
$$\sigma_k^2 = (1 - |a_{kk}|^2) \sigma_{k-1}^2 . \quad (\text{A.8})$$

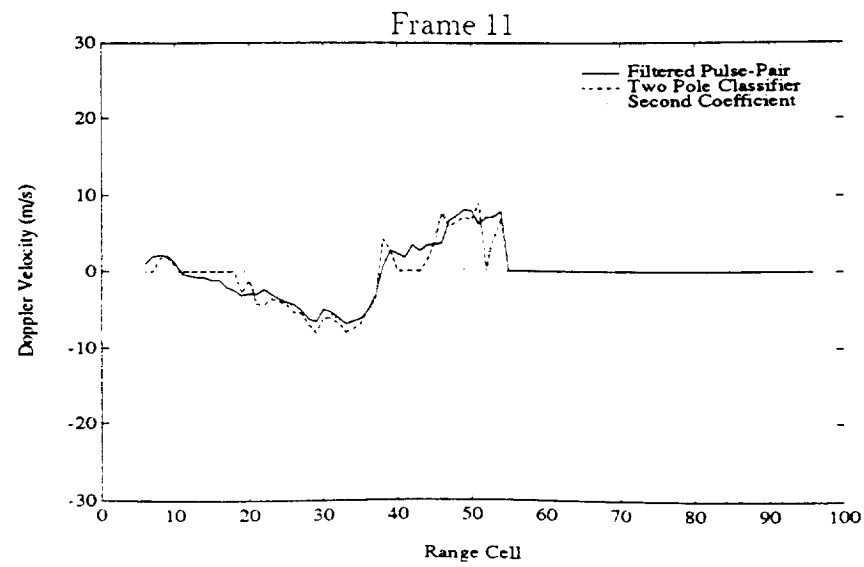
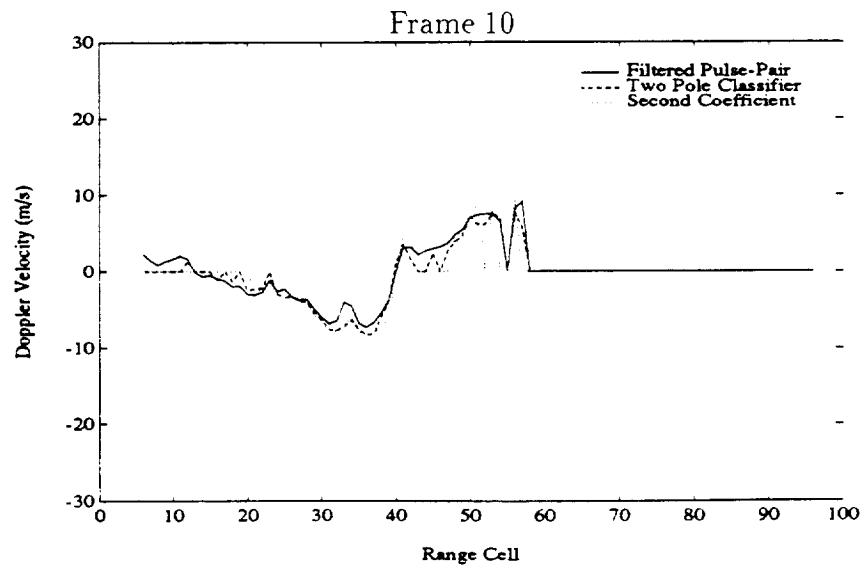
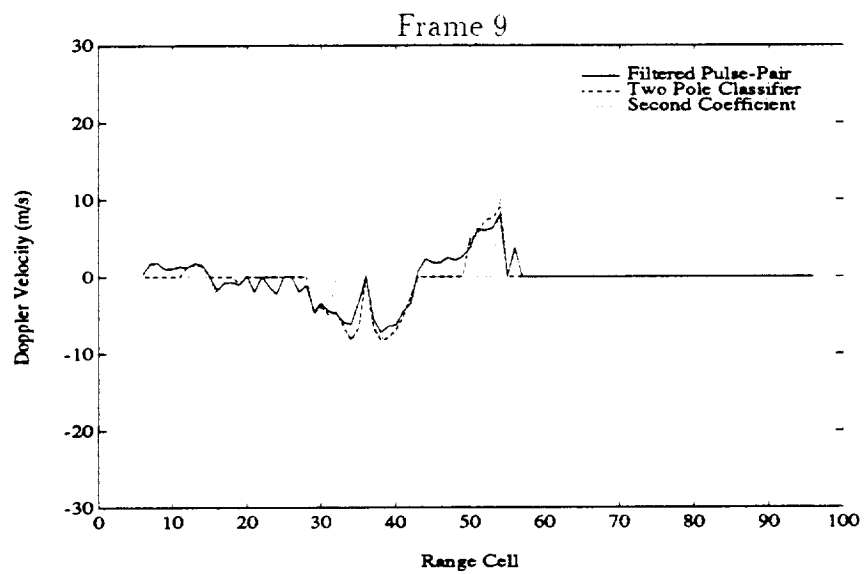
The recursive nature of the Levinson-Durbin algorithm has the advantage of computing not only the AR coefficients for the given model order, but also for all lower order models as well, which can help in the determination of the correct model order.

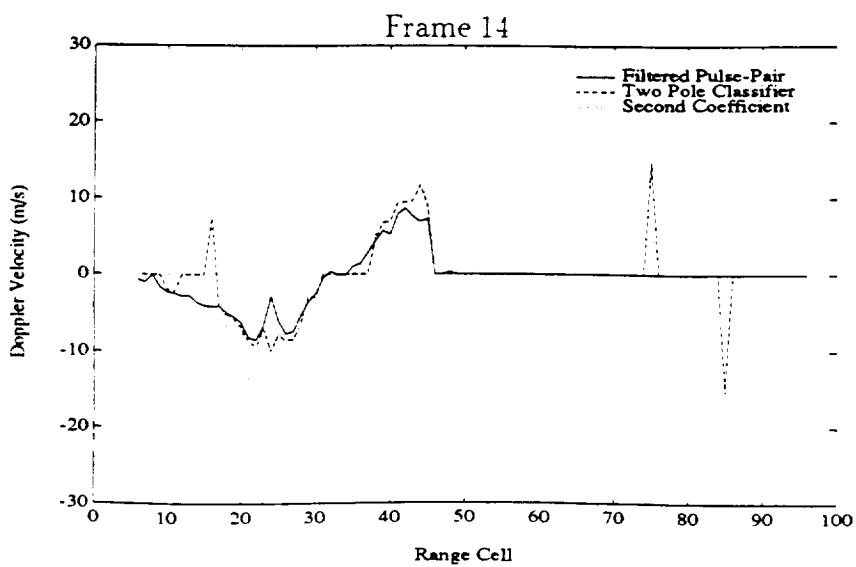
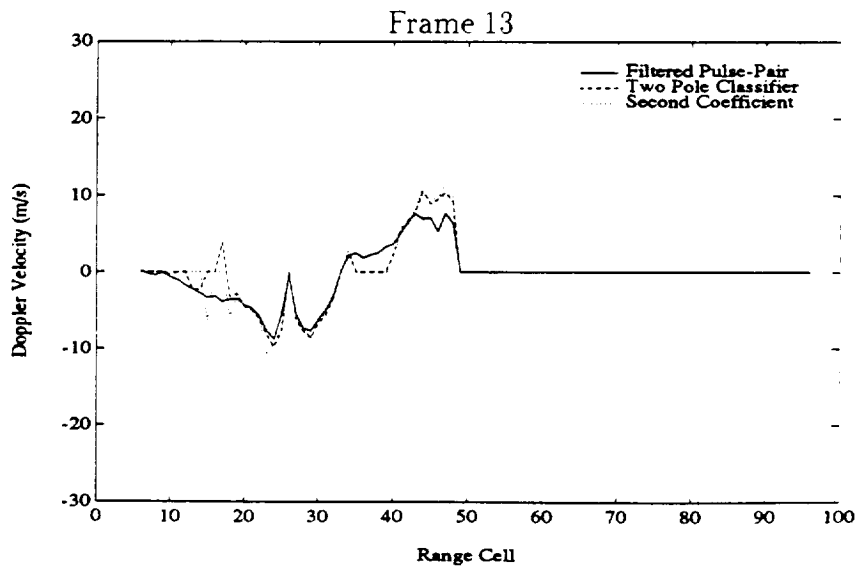
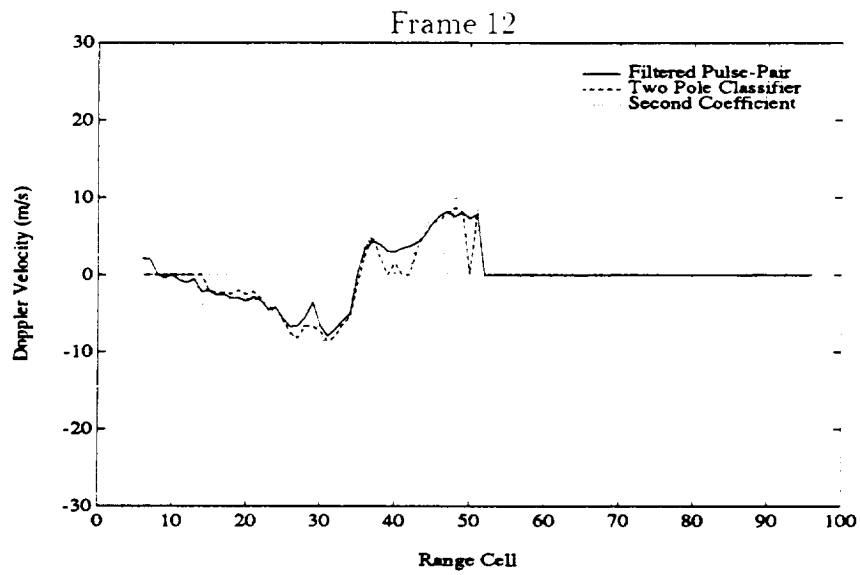
Appendix B
Windspeed Estimates By Frame

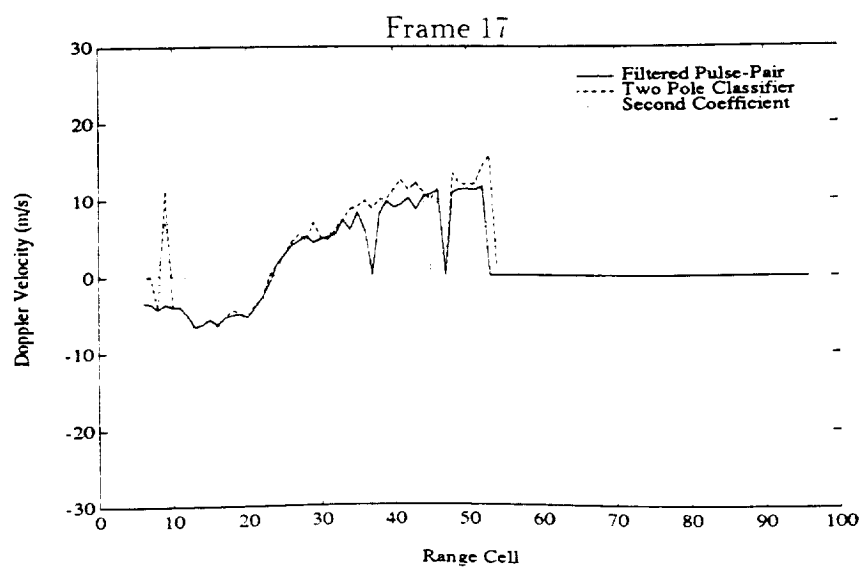
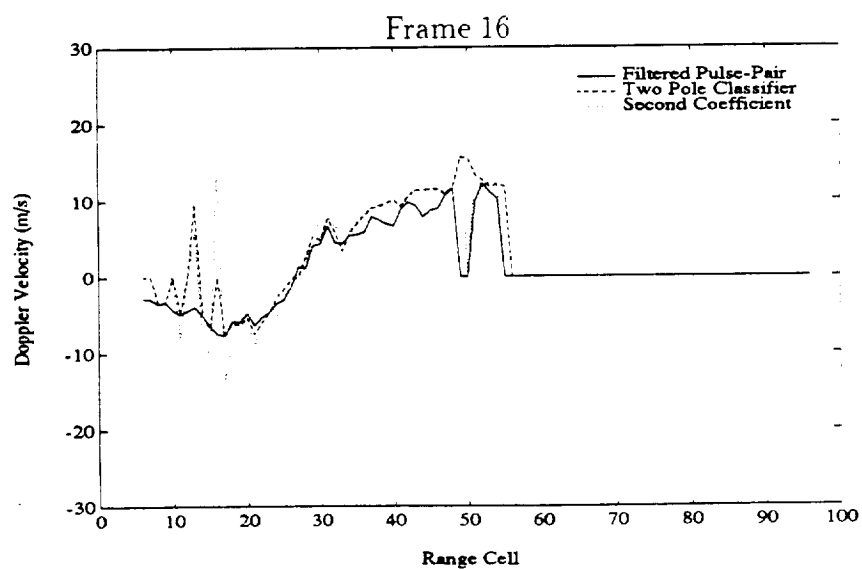
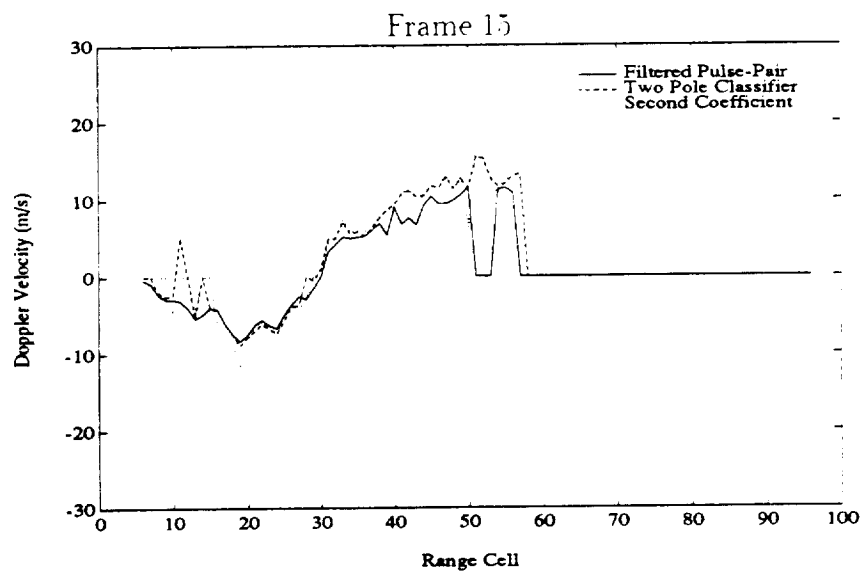


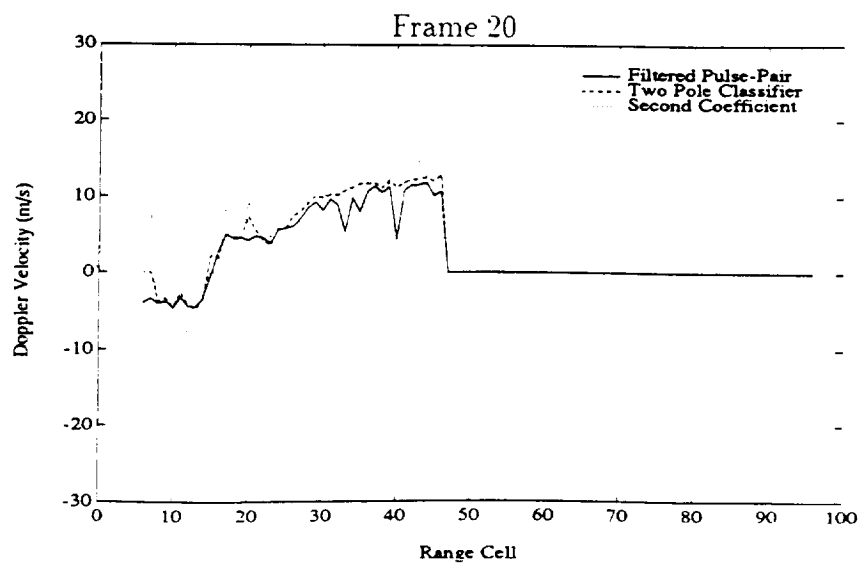
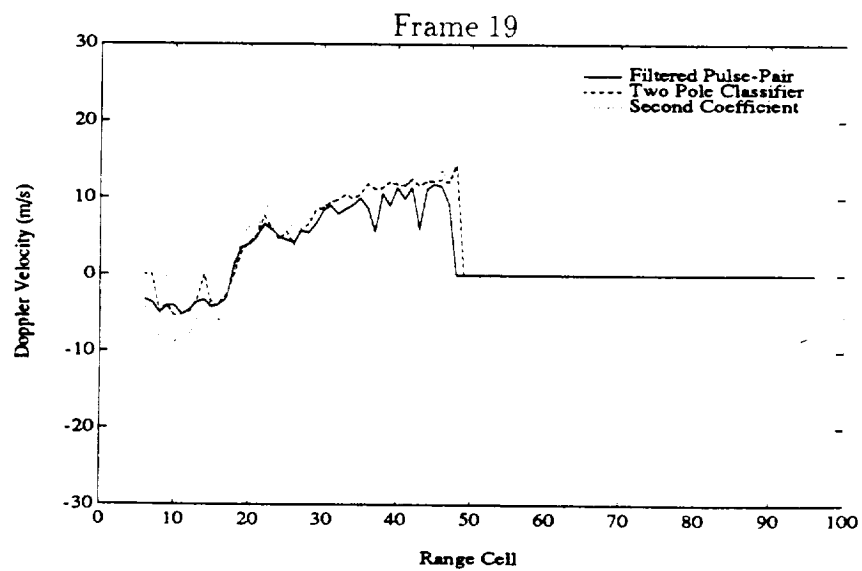
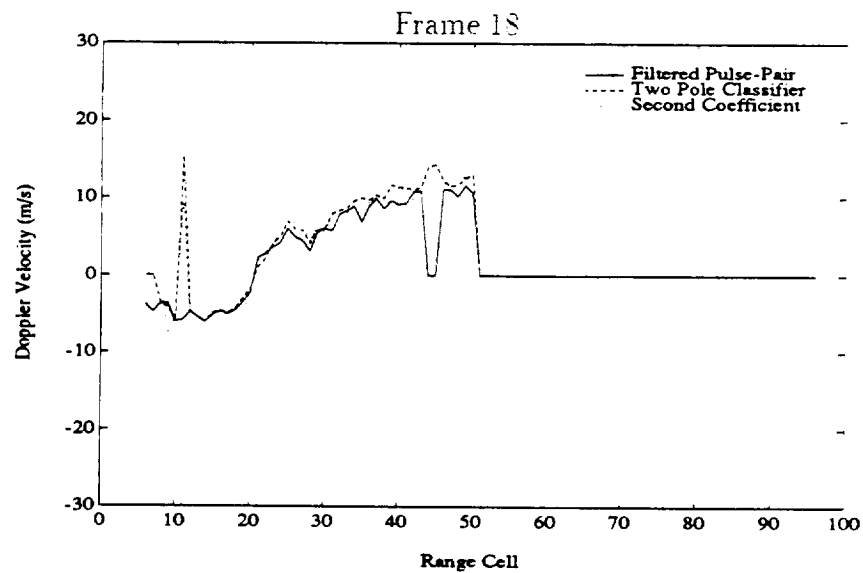


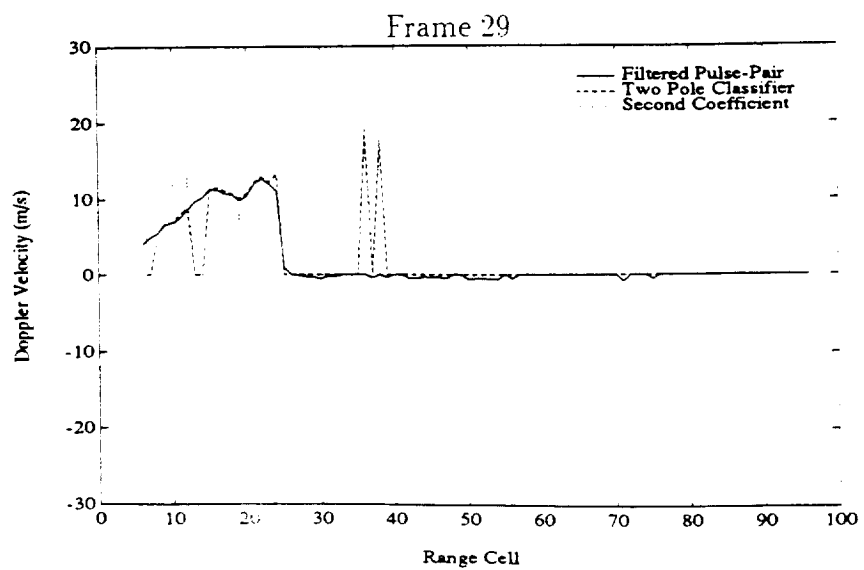
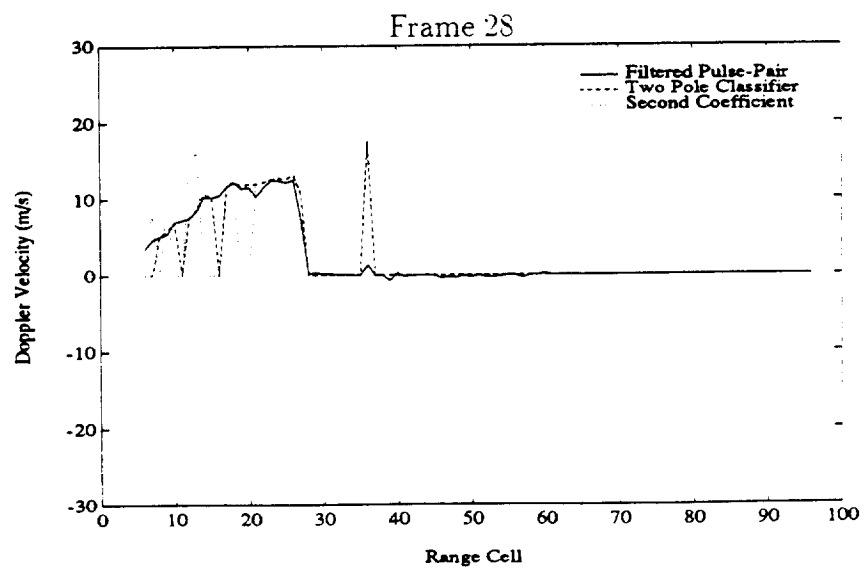
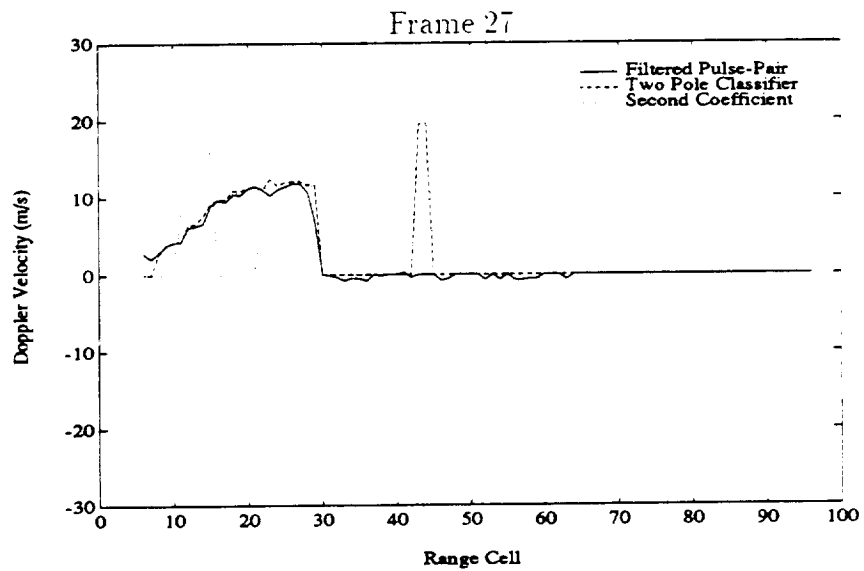


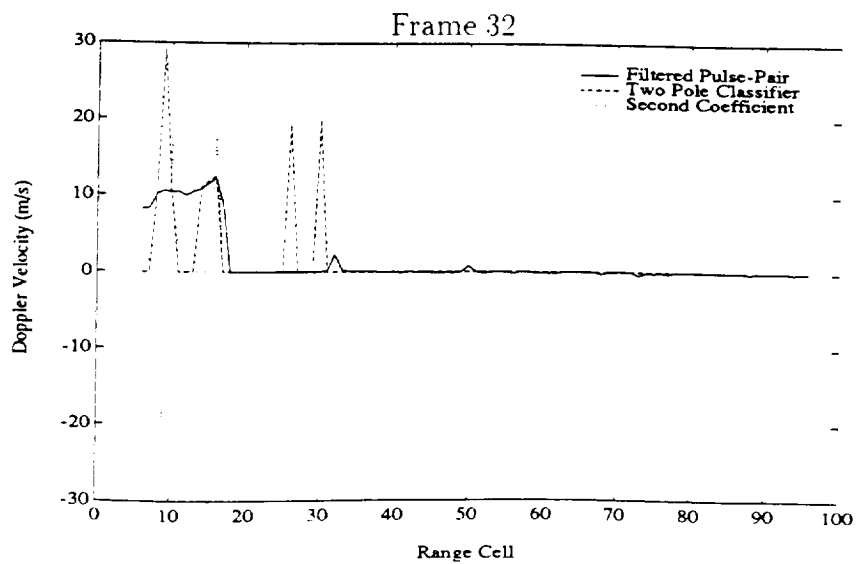
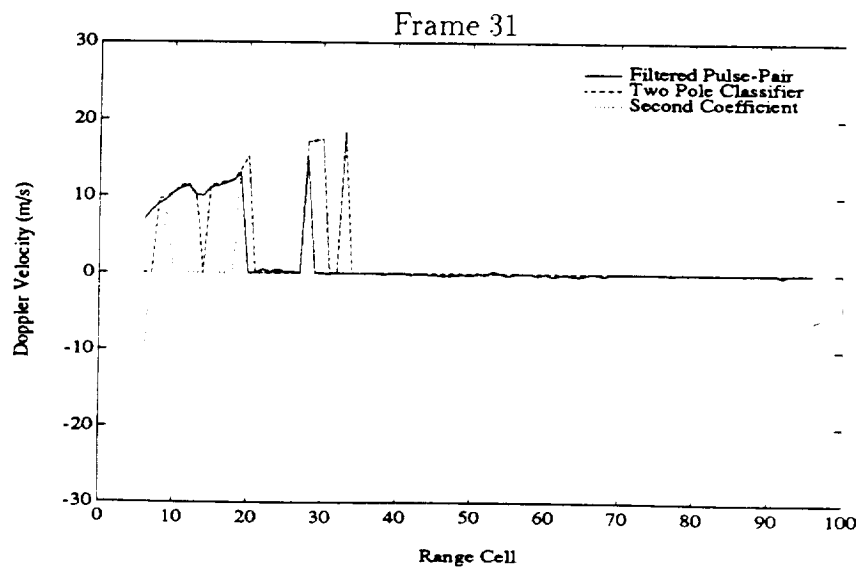
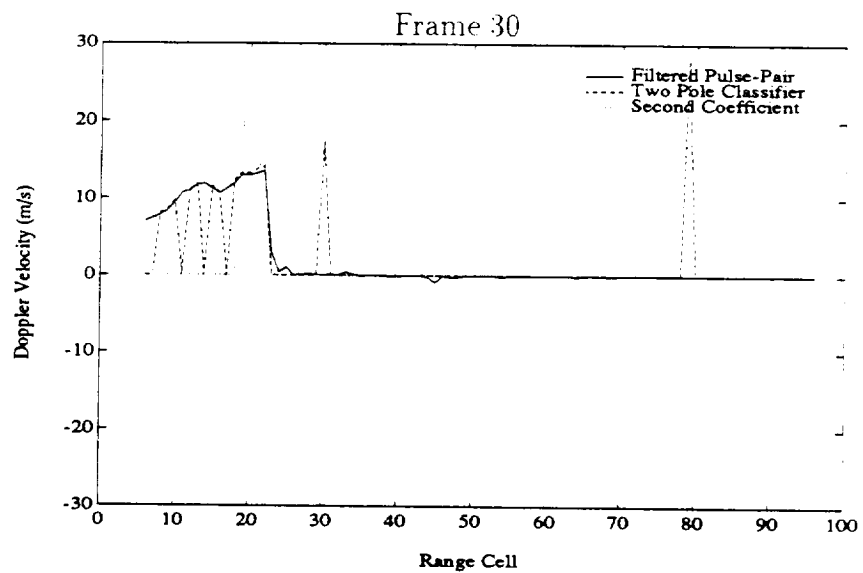


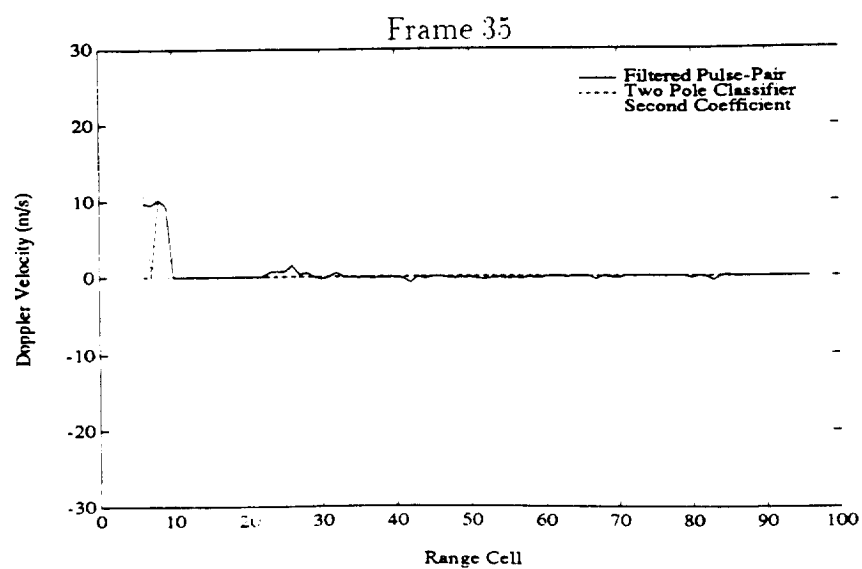
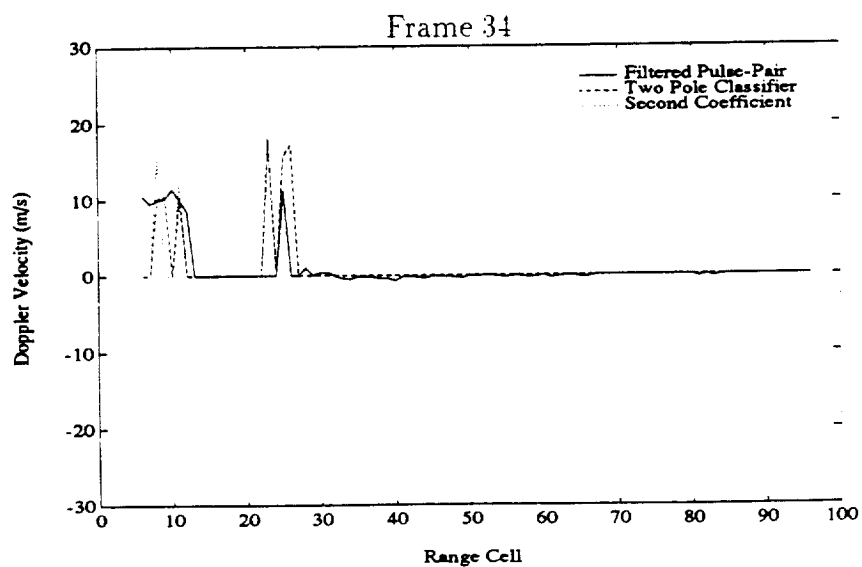
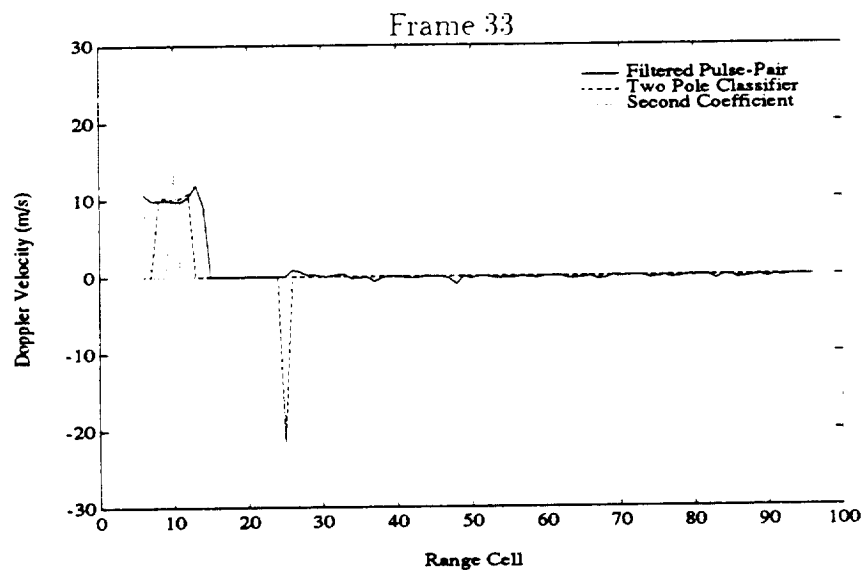


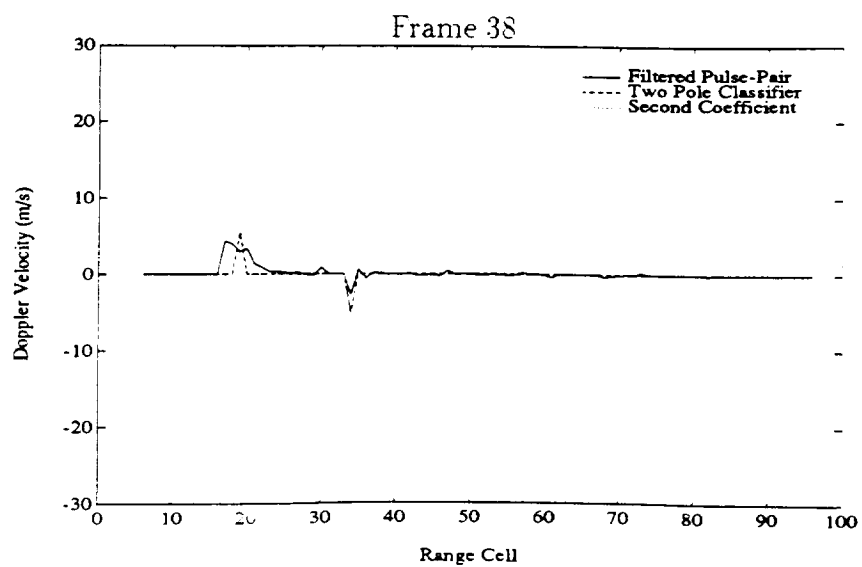
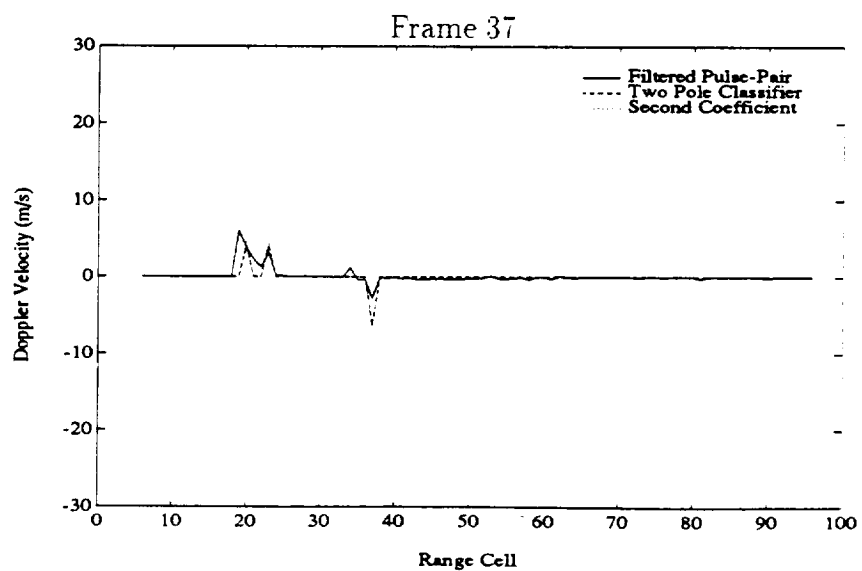
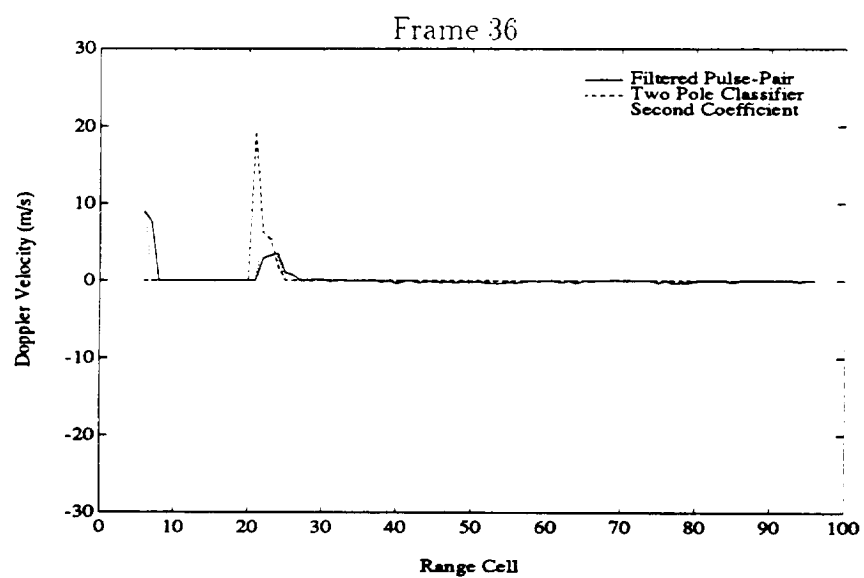


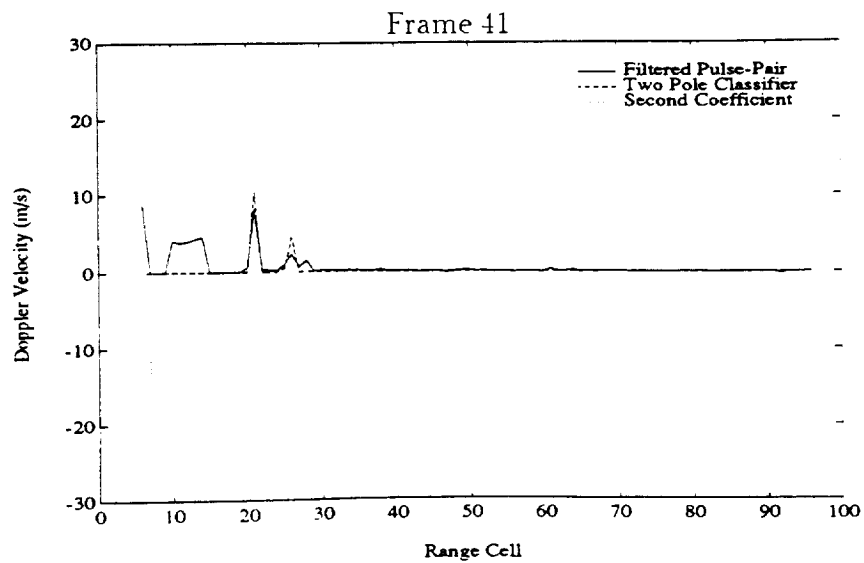
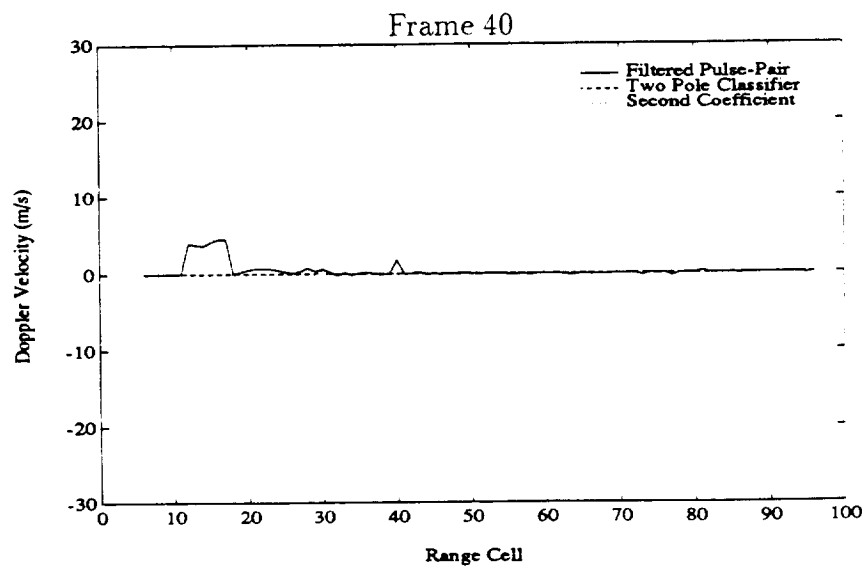
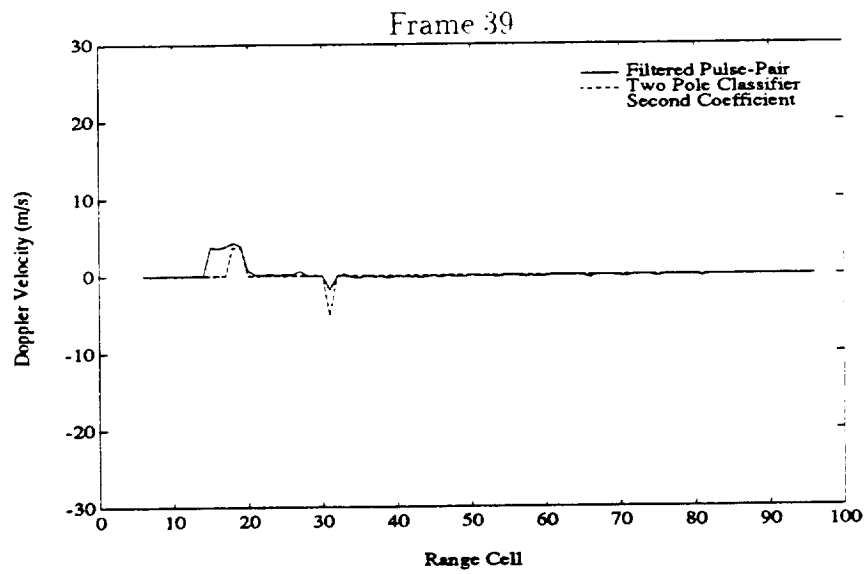


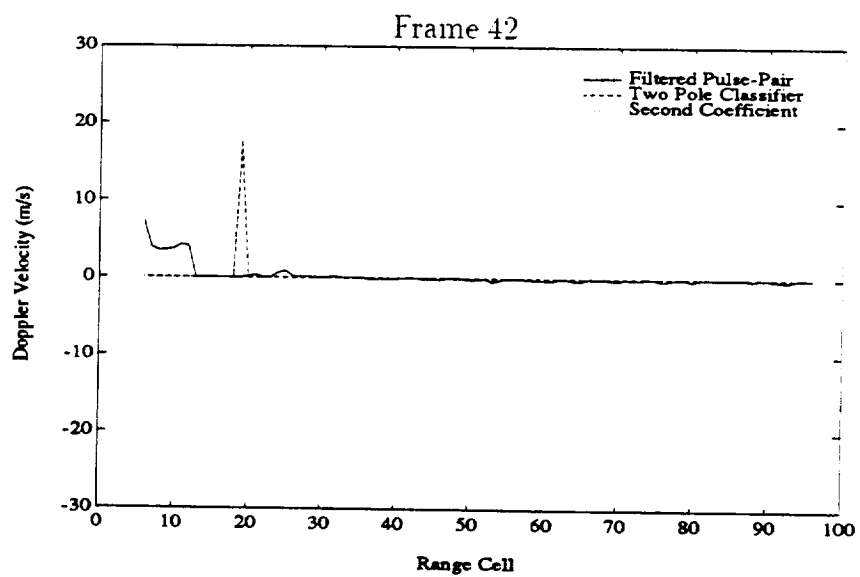












14. Lonnie C. Ludeman. *Fundamentals of Digital Signal Processing*. Harper and Row, New York, 1986.
15. A. V. Oppenheim and R.W. Schaffer. *Discrete-Time Signal Processing*. Prentice Hall, Englewood Cliffs, New Jersey, 1989.
16. S. M. Kay and S. L. Marple. "Spectrum Analysis—A Modern Perspective". *Proceedings of the IEEE*, vol. 69, no. 11, November 1981, pp. 1380–1419.
17. F. B. Hildebrand. *Introduction to Numerical Analysis*. McGraw-Hill, New York, 1956.
18. R. N. McDonough and W. H. Huggins. "Best Least-Squares Representation of Signals by Exponentials". *IEEE Trans. Autom. Control*, vol. 13, August 1968, pp. 408–412.
19. E. G. Baxa, Jr. "Airborne Pulsed Doppler Radar Detection of Low-Altitude Windshear — A Signal Processing Problem". *Digital Signal Processing*, vol. 1, no. 4, October 1991, pp. 186–197.
20. H. W. Schlickemaier. "Windshear Casy Study: Denver, Colorado, July 11, 1988". Technical Report DOT/FAA/DS-89/19, report available through National Technical Information Service, Springfield, Virginia, November 1989.
21. Robert Schalkoff. *Pattern Recognition: Statistical, Structural, and Neural Approaches*. John Wiley and Sons, New York, 1992.

END DATE

OCT 1, 1992